Geophysical Research Letters

RESEARCH LETTER
10.1029/2024GL113880

Limited Shallow Slip in the 1938 M_S 8.3 Alaska Peninsula Earthquake Rupture

Yefei Bai[1,2], Honghuan Zhi[1], Thorne Lay[3], Chengli Liu[4], Lingling Ye[5], and Kwok Fai Cheung[6]

[1]Ocean College, Zhejiang University, Zhoushan, China, [2]Hainan Institute, Zhejiang University, Sanya, China, [3]Department of Earth and Planetary Sciences, University of California, Santa Cruz, CA, USA, [4]School of Geophysics and Geomatics, China University of Geosciences, Wuhan, China, [5]Department of Earth and Space Sciences, Southern University of Science and Technology, Shenzhen, China, [6]Department of Ocean and Resources Engineering, University of Hawaii at Manoa, Honolulu, CA, USA

Key Points:

- North Pacific tide gauge recordings of tsunami for the 1938 earthquake are modeled to constrain the coseismic large-slip distribution
- Large slip is concentrated further northeast on the down-dip megathrust than for the overlapping 2021 Chignik M_W 8.2 earthquake
- Tsunami amplitudes and frequency content indicate that only minor (~1.0 m) coseismic slip extends up-dip shallower than ~20 km

Supporting Information:

Supporting Information may be found in the online version of this article.

Correspondence to:

Y. Bai and L. Ye,
yfbai@zju.edu.cn;
yell@sustech.edu.cn

Citation:

Bai, Y., Zhi, H., Lay, T., Liu, C., Ye, L., & Cheung, K. F. (2025). Limited shallow slip in the 1938 M_S 8.3 Alaska Peninsula earthquake rupture. *Geophysical Research Letters*, *52*, e2024GL113880. https://doi.org/10.1029/2024GL113880

Received 27 NOV 2024
Accepted 31 JAN 2025

Author Contributions:

Conceptualization: Yefei Bai, Thorne Lay, Lingling Ye, Kwok Fai Cheung
Data curation: Honghuan Zhi, Chengli Liu, Kwok Fai Cheung
Formal analysis: Yefei Bai, Chengli Liu
Funding acquisition: Yefei Bai, Thorne Lay, Chengli Liu
Investigation: Yefei Bai, Honghuan Zhi, Thorne Lay, Lingling Ye
Methodology: Yefei Bai, Thorne Lay, Chengli Liu, Lingling Ye
Resources: Kwok Fai Cheung
Software: Yefei Bai, Honghuan Zhi
Validation: Yefei Bai

Abstract The 1938 M_S 8.3 and 2021 M_W 8.2 earthquakes both ruptured within the Semidi segment of the Aleutian-Alaska subduction zone. The large-slip distribution of the 2021 event is well constrained within the depth range 25–45 km, with seaward tsunami observations excluding significant shallower coseismic slip. The 1938 event slip distribution is more uncertain. Regional and far-field tide gauge observations for the 1938 event are modeled to constrain the location of large coseismic slip. The largest slip (2.0 m) is located below the continental shelf on a 180-km-long portion of the rupture extending further northeast than the 2021 rupture, to near Sitkinak Island. Minor slip (1.0 m) extends seaward under the continental slope to 8 km deep, where large slip may have occurred in 1788. The megathrust shallower than 25 km depth to the southwest experienced many small aftershocks and aseismic slip following the 2021 event, and has limited slip deficit.

Plain Language Summary Overlapping very large earthquakes ruptured on the subduction zone plate boundary along the Alaska Peninsula in 1938 and 2021, generating moderate tsunamis that reached the North American coastline and Hawaii. Prior modeling of seismic, geodetic and tsunami recordings indicates that the 2021 event primarily ruptured the depth range 25–45 km. It has been proposed that the 1938 rupture extended further northeast than the 2021, which reached to near Chirikof Island, and possibly to shallower depth. Modeling tide gauge recordings of the 1938 tsunami in the north Pacific supports the 1938 rupture extending as far northeast as Sitkinak Island with 2 m slip in the depth range 20–52 km, along with 1 m slip in the depth range 8–20 km. The 1938 and 2021 rupture zones overlap, but these are not precisely repeating events. The weak shallow slip in the 1938 event overlaps the likely area of larger slip in an event in 1788.

1. Introduction

Subduction zone megathrust faults accommodate plate convergence through a combination of seismic and aseismic slip with both along-strike and along-dip variations (e.g., Lay et al., 2012; Kanamori, 2014). With large underthrusting earthquakes typically having coseismic large-slip zones within the depth range 15–45 km, there is particular interest in the slip behavior of the shallow megathrust from the trench down to ~15 km depth. For some great earthquakes, such as the 2010 Maule, Chile, 2011 Tohoku, Japan, and 2015 Illapel, Chile events, portions of the shallow megathrust failed co-seismically, with significant enhancement of the resulting tsunami. Other great earthquakes, such as the 2005 Nias, Sumatra, 2007 Bengkulu, Sumatra, and 2014 Iquique, Chile earthquakes, did not rupture the shallow megathrust and were less tsunamigenic. The plate interface located up-dip of the 2007 Bengkulu event subsequently ruptured in the 2010 Mentawai and 18 November 2022 Sumatra earthquakes (e.g., Lay et al., 2011; Hill et al., 2012; Yue et al., 2014; Xia et al., 2024). In some cases, the shallow megathrust fails spontaneously without being preceded by deeper ruptures, as in the 1992 Nicaragua, and 1994 and 2006 Java earthquakes, and in some regions no large shallow events have been documented (e.g., Xia et al., 2024). When the shallow megathrust ruptures with large slip under deep water, particularly strong excitation of tsunami results, leading to such events being designated as tsunami earthquakes (Kanamori, 1972; Lay & Bilek, 2007).

When large megathrust earthquakes occur, determining the up-dip limit of slip is important for establishing whether the potential remains for a damaging tsunami earthquake in the shallow megathrust. Determination of the up-dip limit of slip is challenging, given the landward location of regional seismic and geodetic stations, but the situation for events in recent decades is much improved by the availability of seaward tsunami recordings,

Visualization: Yefei Bai, Honghuan Zhi, Thorne Lay, Chengli Liu
Writing – original draft: Yefei Bai, Thorne Lay, Lingling Ye, Kwok Fai Cheung

primarily from seafloor pressure sensors such as the NOAA DART (Deep-ocean Assessment and Reporting of Tsunamis) system. Modeling of the tsunami arrival times and waveforms at seaward locations can provide ∼10 km bounds on the up-dip limit of significant (>∼1 m) coseismic slip for large events. For two large recent megathrust earthquakes along the Alaska Peninsula (Figure 1), the up-dip limit of coseismic large slip has been well-constrained to be no shallower than 20–25 km by analyses including tsunami observations. These are the 2020 Simeonof M_W 7.8 rupture in the Shumagin segment (e.g., Bai et al., 2022; Mulia, Heidarzadeh, & Satake, 2022; Ye et al., 2021), and the 2021 Chignik M_W 8.2 rupture in the adjacent Semidi segment (e.g., Mulia, Gusman, et al., 2022; Liu et al., 2023; Ye et al., 2022), with afterslip and aftershock activity extending seaward of the coseismic large-slip zones. Evidence for a possible shallow slow slip event in 2018 seaward of the 2021 rupture zone (He et al., 2023) and analysis of GNSS-A seafloor geodetic stations support the lack of shallow coseismic slip in these events (Brooks et al., 2023; DeSanto et al., 2023). Geodetic inferences from land-based stations have indicated limited slip deficit along the Shumagin segment and the possibility of strong locking of the shallow megathrust along the Semidi segment (e.g, S. Li & Freymueller, 2018), particularly toward the northeastern end (e.g., Drooff & Freymueller, 2021; Xiao et al., 2021; Wang et al., 2024), although such inferences are non-unique and deeper patchy coupling can match the data as well (e.g., Zhao et al., 2022). Marine reflection seismology has imaged irregular, but concentrated (<200 m depth extent) reflectivity of the shallow megathrust along both segments. This has been interpreted as favoring seismogenic potential (Shillington et al., 2022). So, the issue is, as yet, unresolved.

On 10 November 1938, a portion of the Semidi megathrust segment (Figure 1) ruptured in an M_S 8.3 (Gutenberg & Richter, 1949), M_W 8.3 (Estabrook et al., 1994) earthquake (USGS-National Earthquake Information Service: 20:18:49 UTC, 55.178°N 158.181°W). The sparse relocated aftershock zone was inferred to extend to near the trench (Sykes, 1971; Sykes et al., 1981), but recent relocations (Figure 1) indicate that it was concentrated further down-dip (Tape & Lomax, 2022). Aftershocks are known to be, at best, rough indicators of where coseismic large slip occurred in major earthquakes, so these results are ambiguous with respect to shallow slip in the 1938 event. Analysis of tsunami tide gauge recordings by Johnson & Satake (1994) indicates that large slip overlaps and extends slightly further northeast along-strike than the large-slip region for the 2021 Chignik earthquake (Figure 1), and seismic wave analyses support concentration of slip in the northeastern portion of the down-dip rupture zone (Figure 1) (Estabrook et al., 1994; Ye et al., 2022). However, Freymueller et al. (2021) modeled two tide gauge recordings for the 1938 event at opposite azimuths along the rupture strike, favoring a model with up to 3 m of slip extending up-dip beneath the trench slope almost to the trench and along-strike to near Sitkinak Island (Figure 1). Here we model a larger set of available tsunami tide gauge recordings to re-evaluate the distribution of large slip in 1938 and we assess the potential for a shallow tsunami earthquake in the Semidi segment.

2. Materials and Methods

Regional and far-field tsunami recordings at tide gauges in the northern Pacific are modeled to constrain the distribution of large slip during the 1938 earthquake. The well-established non-hydrostatic tsunami modeling code NEOWAVE (Yamazaki, Cheung, & Kowalik, 2011; Yamazaki, Lay, et al., 2011; Yamazaki et al., 2009) is used for all computations. The model is built upon the depth-integrated non-hydrostatic free-surface flow system (Bai et al., 2018) with extension to include kinematic seafloor deformation and spherical coordinate system (Yamazaki et al., 2023). The performance has been comprehensively verified through theoretical analysis, numerical investigation, and benchmarking studies (Bai & Cheung, 2013, 2015, 2016, 2018; Bai et al., 2015b; L. Li & Cheung, 2019; Yamazaki et al., 2012; Wei et al., 2024). The model has been utilized to investigate earthquake and tsunami sources, near and far-field wave dynamics, and coastal inundation processes in historical and hypothetical events (Bai et al., 2015a, 2017, 2022, 2023; Cheung et al., 2013; Lay et al., 2013; L. Li, Lay, et al., 2016; L. Li, Cheung, et al., 2016; Liu et al., 2023, 2024; Yamazaki et al., 2018, 2021, 2024; Yamazaki, Lay, et al., 2011; Yamazaki, Cheung, & Kowalik, 2011; Ye et al., 2021, 2022).

Up to five levels of two-way nested computational grids are utilized to describe tsunami processes with increasing resolution from the open ocean to the shore near each tide gauge station. Figure 2 illustrates the level-1 grid with 2 arc min (∼3,600 m) resolution extending across the northeast pacific and coverage of the four level-2 grids with 30 arc s (∼925 m) resolution along the Aleutian Islands, Southeast Alaska, U.S. West coast, and the Hawaiian Islands. Nested higher level grids with the finest resolution of 0.3 arc s (∼9.25 m) are used for each tide gauge station (Figures S1–S7 in Supporting Information S1) to capture complex response in harbor or nearshore areas.

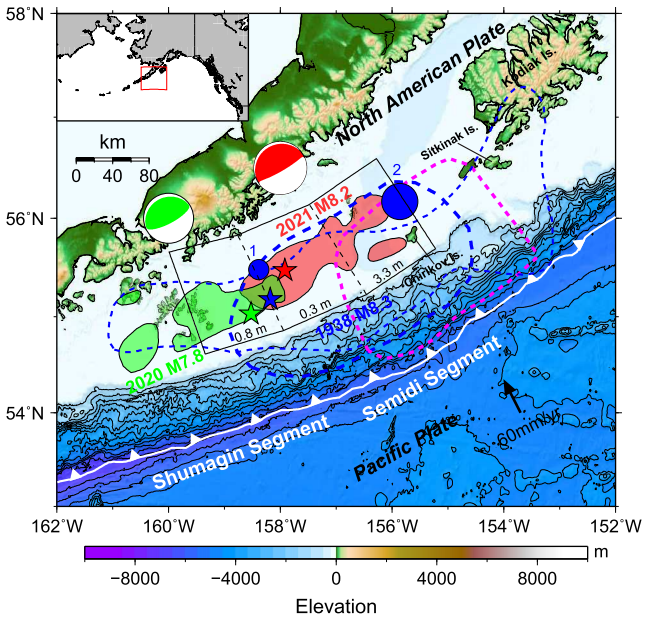

Figure 1. Map of major earthquake ruptures along the Alaska Peninsula region from the Shumagin Islands to Kodiak Island. The inset locates the main map. The 1938 M_S 8.3 epicenter is shown with a blue star and the aftershock zone from Sykes (1971) is indicated with thick blue dashes. The light blue dashes outline the relocated 1938 aftershocks from Tape and Lomax (2022). Three black rectangles indicate the slip region, with indicated uniform slip magnitudes from the tsunami inversion by Johnson and Satake (1994). The blue circles indicate locations of two subevents of the 1938 event, scaled proportional to seismic moment, from body wave inversion by Estabrook et al. (1994). The magenta dashed zone is the 1938 large-slip (>1 m) zone from modeling two tsunami tide gauges by Freymueller et al. (2021). The 2020 Simeonof M_W 7.8 earthquake epicenter (green star), >0.5 m slip regions from Bai et al. (2022) (green patches), and focal mechanism (green lower hemisphere) are shown along with the 2021 Chignik M_W 8.2 earthquake epicenter (red star), >2 m slip region from Liu et al. (2023) (red patches), and focal mechanism (red lower hemisphere). The vector indicates Pacific-North America convergence in the MORVEL model from DeMets et al. (2010). The bathymetry contour ranges from 200- to 7000-m water depth with a 500-m interval.

The time step varies from 1 to 0.05 s through the multi-level grid systems to maintain numerical stability. The computation covers up to 13 hr of elapsed time for full development of resonance oscillations in nearshore or basin areas. A forward modeling approach is conducted to evaluate a series of specified source parameters constrained by the local megathrust geometry until a preferred model is obtained based on fitting of the observed data at each tide gauge, emphasizing the leading tsunami arrivals.

3. Data

3.1. Tide Gauge Data

Long-duration sea-level signals recorded at seven tide gauge stations are considered in this study to provide a comprehensive evaluation on the numerical results. Tide gauge recordings at Unalaska, Sitka, Santa Monica, and Honolulu are digitized from Neumann (1940), and those at Crescent City, San Diego, and San Francisco are re-digitized from Johnson and Satake (1994). Before the 1960s, water levels were recorded on a continuously running pen and ink strip chart with all harmonic components included. The recording at Unalaska is quite noisy and the onset of the first tsunami arrival is ambiguous, as is evident in Freymueller et al. (2021). Tidal constituents, if present, are then high-pass filtered out of the recordings to yield relatively isolated tsunami waveforms with 1-min interval over the still water level for comparison. It is observed that the recorded tsunami waveforms at most stations generally vary within a ±10 cm range except for the Crescent City and San Francisco where a moderate ±20 cm fluctuation is observed.

3.2. Bathymetry Adjustments

The Crescent City harbor has undergone significant modification since the early 20th century because of consecutive large impacts from a series of tsunami events (Dengler & Uslu, 2011). Before 1938, a 1,000 m-long outer breakwater was completed in 1930, and shortly after a tide gauge was established in 1933 on Hobbs Wall Wharf, an early railroad lumber wharf. After 1938, a 370 m-long inner breakwater was added in 1946 to divide the harbor into inner and outer areas. Later on, the tide gauge was relocated to Citizens Dock which was completed in 1950. In order to compute the tsunami waves more precisely, we modify the current DEM data guided by the nautical chart of St. George Reef and Crescent City Harbor in 1938 (U.S. coast and Geodetic Survey) and revert the water depth and harbor configuration back to the historical settings (Figure 2, Figure S3 in Supporting Information S1). Given some uncertainty in the early wharf configuration and inaccuracy of tide gauge recordings of the 1933 Sanriku, Japan tsunami, we compute tsunami at several candidate locations around the current location on Citizen's Dock (41°44.7′N, 124°11.1°W) for a sensitivity analysis.

Located along the south shore of Oahu, Honolulu harbor has also been under steady development over the last century. Differences in entrance position and port layout may lead to different patterns of local tsunami response. We revise the current DEM according to the nautical chart of Honolulu Harbor published in 1941 (U.S. coast and Geodetic Survey) to create a more appropriate computational grid for the 1938 tsunami modeling (Figure S7 in Supporting Information S1).

4. Results

Initial calculations were made for the seven tide gauge waveforms using the slip model of Johnson and Satake (1994), for which the slip and seafloor deformation are shown in Figure 3a. This model was inverted from six of the same tide gauges we use (omitting Crescent City), and features three subfaults 100 km long by 150 km wide with 10° dip and northeastward varying slip of 0.79, 0.3,4 and 3.3 m. The along-strike distribution of slip was not well resolved, but the average slip is 1.5 m, with a seismic moment estimate of 2×10^{21} Nm (M_W 8.13).

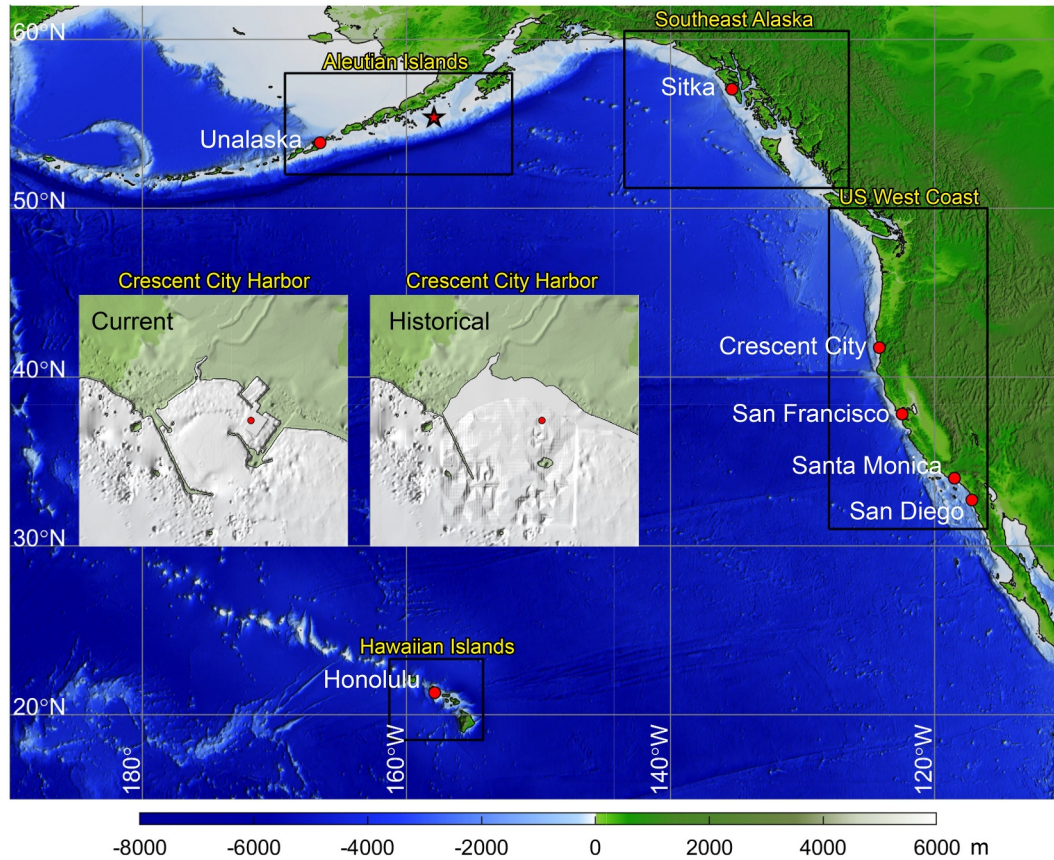

Figure 2. North Pacific Level-1 bathymetry grid and seven tide gauge locations that have recordings modeled for the 1938 tsunami. The insets show restoration of the 1938 harbor configuration at Crescent City. Level-2 grid regions are outlined by rectangles. Nested grid levels used for each tide gauge station calculation are shown in Figures S1–S7 in Supporting Information S1. Honolulu harbor also required historical restoration to the configuration prior to airport construction (Figure S7 in Supporting Information S1).

Our waveform fits for this model (Figure 4a) show reasonable amplitude at all stations, but too late of arrivals at Sitka and San Francisco. Generally, approximations often made in trans-oceanic tsunami modeling (neglect of solid Earth elasticity, salinity gradients, and gravity changes) tend to cause early first arrival predictions with minor waveform distortion (e.g., Allgeyer & Cummins, 2014; Baba et al., 2017; Fujii et al., 2021; Tsai et al., 2013; Watada, 2023; Watada et al., 2014). We apply uniform time shifts to the more distant tide gauge calculations to compare with the observations to offset the primary effect of the computational limitations.

The late arrival at Sitka was focused on by Freymueller et al. (2021), which modeled that waveform and the noisy Unalaska waveform to produce a "far eastern" slip model shown in Figure 3b. This model has large slip concentrated further northeastward than the large-slip patch in Johnson and Satake (1994), extending to near Sitkinak Island and also extending seaward to near the trench, as shallow slip is required to make the signal arrive as at the time observed at Sitka. The slip is as much as 3 m in the northeastern large-slip region, and this large slip extends seaward of the continental break, producing large up-lift along the continental slope (Figure 3b). The occurrence of large slip below the continental slope is known to generate large short-wavelength tsunamis, and was ruled out for the 2020 Simeonof and 2021 Chignik events because such short period tsunami energy was not observed at seaward tide gauge stations (e.g., Bai et al., 2022; Mulia, Heidarzadeh, & Satake, 2022; Mulia, Gusman, et al., 2022; Liu et al., 2023; Ye et al., 2021, 2022). Our tsunami waveform predictions for the Freymueller et al. (2021) model (Figure 4b) show the expected strong short period tsunami signals at seaward locations, notably at Crescent City, San Francisco, Santa Monica and San Diego, which are not apparent in the data. The first arrival time at Sitka is indeed well-matched for this model, but there are later short period arrivals with excessive strength. Calculations for the 2021 Chignik earthquake down-dip slip models of Liu et al. (2023)

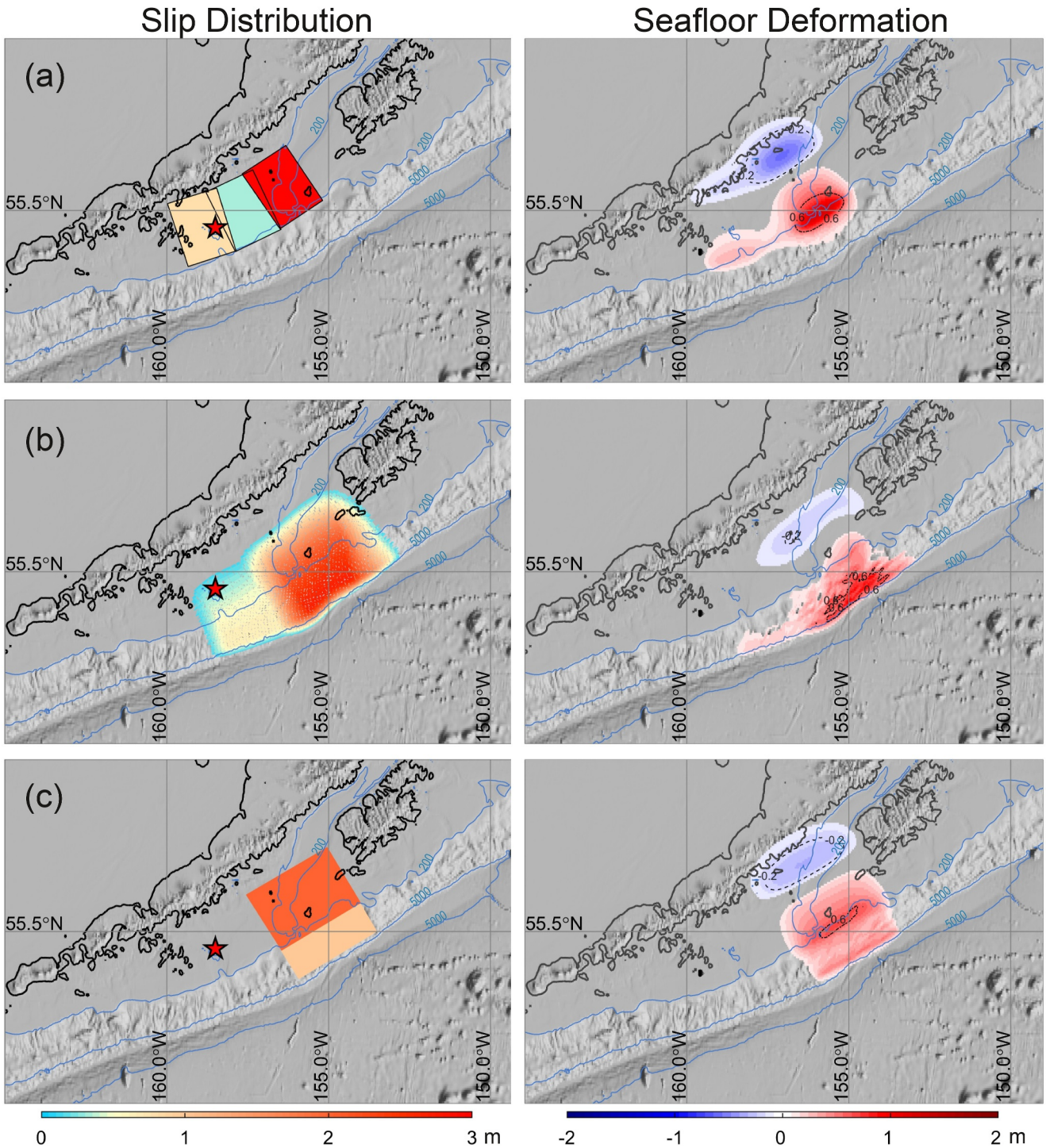

Figure 3. 1938 earthquake slip distributions (left column) and computed seafloor deformation (right column) for the models of (a) Johnson and Satake (1994), (b) Freymueller et al. (2021) far-east, and (c) the updated preferred 1938 model in this study, which has only 1 m of slip beyond the shelf break and less uplift of the continental slope in contrast to 3 m of shallow slip in the Freymueller et al. (2021) model.

(Figure S8 in Supporting Information S1) and Ye et al. (2022) (Figure S9 in Supporting Information S1) do not have excessive short period tsunami arrivals relative to the 1938 observations, but do predict very late arrivals at Sitka.

Figure 4. Comparison of observed tsunami waveforms and spectra (black lines) from the seven tide gauge stations in Figure 2 with corresponding calculations for the three slip models for the 1938 event in Figure 3 (red lines). Time shifts of the indicated amount have been applied to the computed tsunami signals at large distances.

To improve the overall fit to the full set of observed data, we searched over 57 models with varying geometry and slip, perturbing from the initial configurations of Johnson and Satake (1994) and Freymueller et al. (2021) and seeking the simplest model to fit the data. We find support for the basic northeastward extension of the earlier model advocated by Freymueller et al. (2021) in order to match the arrival time at Sitka (this is still dependent on adequacy of the bathymetric model), but in order to reduce the overprediction of short-period tsunami waves at

seaward stations, the shallow slip on the megathrust must be reduced to about 1 m, with 2 m of slip at greater depth in the northeastern section. This results in our preferred model in Figure 3c, which still has some uplift along the continental slope, but it is much weaker than that for the Far East rupture model of Freymueller et al. (2021). The preferred model produces very good fits to stations along the west coast of North America (Figure 4c), including arrival time at Sitka and appropriate frequency content at Crescent City, San Francisco, Santa Monica, and San Diego. The fit to the initial arrival at Honolulu is good, slightly better for the Johnson & Satake (1994) model (Figure 4a), for our favored model (Figure 4c), but for all three models in Figure 3, secondary arrivals have lower amplitude than the data, possibly due to underestimated oscillations in the complex harbor basin reconstructed from limited bathymetry. This is not improved by including weak slip like that in the western part of the Johnson & Satake (1994) model. The spectral peak at a period of 25 min is least over-estimated by our favored model (Figure 4c). The Unalaska signal, which includes background oscillations evident before the tsunami arrival, can only provide a reference for evaluation of the computed waveform amplitudes.

Results for several slip models that bracket the preferred model are shown in Supporting Information S1. These models have 2 m slip in the deeper segment as in the preferred model but with zero slip in the shallow segment (Figure S10 in Supporting Information S1), 0.5 m slip in the shallow segment (Figure S11 in Supporting Information S1), 1.5 m slip in the shallow segment (Figure S12 in Supporting Information S1), and 1.0 m slip in a shallow segment with only half the width (Figure S13 in Supporting Information S1). For a model with no shallow slip (Figure S10 in Supporting Information S1) the arrival at Sitka is late compared to the preferred model (Figure 4c). With 0.5 m shallow slip (Figure S11 in Supporting Information S1), the period of the first arrivals at Sitka, San Francisco and San Diego is not as well matched as for the preferred model, while with 1.5 m shallow slip (Figure S12 in Supporting Information S1), excessive short-period energy is excited at Crescent City, San Diego and Honolulu; supporting the preferred model with 1.0 m shallow slip (Figure 4c). Reducing the width of the shallow segment with 1 m slip underestimates the period of the first arrival at Santa Monica and San Diego, supporting the up-dip extent of the preferred model.

Our simple 2-subfault model has 14° dip in the deeper segment with 2 m slip over a 180 km length and 130 km width at depths from 20 to 52 km, and 10° dip in the shallower segment with 1 m slip over a 180 km length and 65 km width at depths from 8 to 20 km. Both segments have strike 240° and rake 90°. This model overlaps about half of the 2021 Chignik rupture, but has a northeastern edge extending below Chirikof Island to near Sitkinak Island (Figure 1). Sitkinak did not have any vertical motion documented during 1938 (Brooks et al., 2023), which is consistent with our model deformation (Figure 3c). Once again, we find that the seaward tsunami recordings play a very important role in limiting whether and how much slip occurred below the continental slope due to the increasing short wavelength tsunami excitation in deepening water.

5. Discussion and Conclusions

For our preferred model, if we assume a rigidity of 40 GPa for the deeper segment and 20 GPa for the shallower segment, the total seismic moment estimate is 2.11×10^{21} N-m (M_W 8.15), which is slightly larger than the estimate (2.0×10^{21} N-m; M_W 8.13) of Johnson and Satake (1994). Seismic observations for the 1938 and 2021 ruptures in the Semidi segment were discussed by Ye et al. (2022). The magnitude measures for 1938 include M_S = 8.3 (Gutenberg & Richter, 1949), M_S = 8.39 [ISC], and m_B 8.2 (Abe, 1981). For the 2021 event Ye et al. (2022) compute M_S = 8.1 and m_B = 7.7. The body wave and surface wave analyses of Estabrook et al. (1994) give larger seismic moment estimates, ranging from 2.95 to 6.05×10^{21} N-m, which exceed the tsunami-based estimates, but there is substantial scatter in the waveform comparisons. Our seismic moment estimate would increase for larger choices of rigidity, but some discrepancy remains. Comparison of a Benioff 1–90 recording from Pasadena, California for the 1938 event with an instrument-equalized broadband recording for 2021 indicates comparable amplitude signals, but there is a strong secondary arrival near 60 s for the 1938 event not seen in the 2021 recording. This corresponds to a strong second pulse determined by Estabrook et al. (1994) in a two-subevent model for the 1938 event which places a dominant second event 60 s after the rupture onset about 178-km to the northeast of the epicenter (Figure 1) at the northeast edge of the tsunami rupture model of Johnson and Satake (1994), and centered within the down-dip 2 m slip patch in our preferred model. This late dominant event is evident in the moment rate functions obtained by Estabrook et al. (1994) and Hartzell & Heaton (1985), and no corresponding feature is evident after 60 s in the moment rate function for the 2021 event. Relatively weak energy in the *P* waveforms and the moment rate functions is apparent in the first 60 s of rupture, so small slip does appear to have occurred where the 1938 and 2021 events overlap from their epicenters to 180 km to the northeast, but this

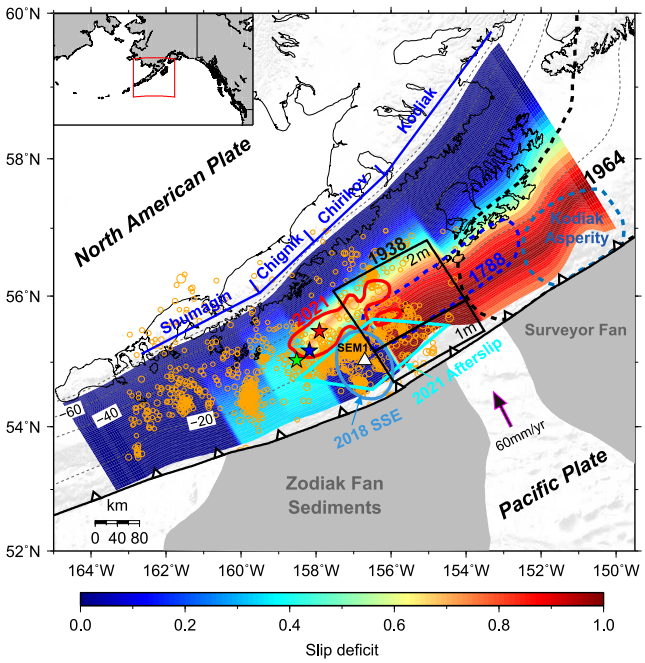

Figure 5. Summary map showing 2021 slip zone from Liu et al. (2023) outlined in red with the red star indicating the epicenter, a green star indicating the epicenter of the 2020 Simeonof event, a blue star indicating the epicenter of the 1938 rupture, our preferred slip model for 1938 (black rectangles with 2 m deeper slip and 1 m shallower slip), aftershocks for 2020 and 2021 events, location of GNSS-A site (white triangle) and triangular areas with 2021 afterslip (Brooks et al., 2023), purple oval shows location of a 2018 slow slip event (He et al., 2023). Suggested 1788 rupture zone (dark blue dashed outline), adapted from Brooks et al. (2023) to extend only in the Kodiak and Chirikof segments, and the slip deficit model from Wang et al. (2024). The large shallow slip region of the Kodiak asperity in the 1964 rupture zone (Suleimani & Freymueller, 2020) is indicated.

was not large enough to be strongly tsunamigenic, as indicated by the model of Johnson and Satake (1994) and our preferred model, which omits the small slip as it is not resolved by the tsunami signals. Chirikof Island is located above the deeper large-slip zone, and should have experienced about 40 cm uplift along with large tsunami inundation (Figure S14 in Supporting Information S1). A local high tsunami runup of >10 m on Chirikof was speculated by Nelson et al. (2015), but we have not computed the local runup, given that the observation in uncertain.

Acquisto et al. (2024) imaged 3D crustal P-wave velocity structure in the Semidi segment and along Kodiak Island, finding strong contrasts in the up-dip limit and increasing width of the dynamic backstop between the western Semidi segment and the Kodiak segment. High velocities are found in the mid-lower forearc crust near the location of large slip in the 2021 Chignik event. The incoming Pacific plate along the eastern Semidi segment has relatively low sediment thickness as it lies between the Zodiac and Surveyor Fans, but the geometry of the subducted sediments is debated. Wang et al. (2024) imaged high V_P/V_S ratios in the vicinity of the 2020 Simeonof rupture and moderate/variable ratios near the 2021 Chignik and 1938 ruptures. They propose that along-strike variation in interseismic megathrust behavior is controlled by changes in fluid content, primarily in the overriding plate above the plate interface from 15 to 35 km deep.

Estimates of geodetically inferred slip deficit in the Semidi segment have been presented by S. Li & Freymueller (2018), Drooff and Freymueller (2021), Xiao et al. (2021), and Wang et al. (2024). These models have rather dramatic differences for the near-trench megathrust up-dip of the 2021 Chignik rupture zone (the western half of the Semidi segment, which Wang et al. (2024) label as the Chignik segment, Figure 5), with early estimates of >60% locking (S. Li & Freymueller, 2018) progressively reducing to near zero slip deficit (Wang et al., 2024), primarily as a result of different assumptions in the modeling (e.g., Xiao et al., 2021) and reflecting the total lack of shallow resolution due to the absence of island measurements. Very low coupling of the region up-dip of the 2021 event is supported by the spotty clustering of shallow aftershocks for the event (e.g., Liu et al., 2023), evidence for 2 and 3 m of afterslip at depths shallow than 20 km from seafloor GNSS_A station SEM1 seaward of the 2021 epicenter (Brooks et al., 2023), and detection of a slow-slip event in 2018 in the same region (He et al., 2023) (Figure 5). We infer that there is little slip deficit in the Chignik segment and hence low probability of having a tsunami earthquake there. The shallow slip deficit along the Chirikof segment (the eastern half of the Semidi segment in Figure 5) between the Chignik and Kodiak segments (Wang et al., 2024) has remained consistently high, near 100% throughout these studies, being controlled by measurements available from Chirikof and Sitkinak Islands, as has that in the Kodiak segment, controlled by measurements from Kodiak. Over the 86 years since the 1938 event, slip deficit of up to 5.2 m could have accumulated in this region, much larger than the 1 m slip in the shallowest part of our preferred 1938 rupture model, so one has to consider earlier ruptures to see if slip can be larger in this region.

Prior to the 1938 event, a large tsunamigenic earthquake occurred on 21 July 1788 leaving tsunami sand deposits on Sitkinak and Chirikof Islands (Briggs et al., 2014; Lander, 1996; Nelson et al., 2015). Sitkinak Island experienced up-lift in 1788, whereas it experienced down-drop in the 1964 Alaska earthquake (Briggs et al., 2014). The 1788 earthquake is inferred to involve rupture reaching to near the trench extending from central Kodiak Island southwest across the entire Semidi segment, possibly to along the Shumagin Islands (e.g., Witter et al., 2014). Such a long rupture would have to have less than 5 m slip along the Shumagin Islands, to account for the absence of geological evidence for vertical displacement on Simeonof Island. Strong tsunami excitation near the trench is expected for several meters of slip, so it is unlikely that shallow megathrust was involved, at least along the Shumagin segment, we infer that rupture probably does not extend beyond the Semidi segment (e.g., Briggs et al., 2014), and likely not across the Chignik segment where weak coupling is now inferred. There is little constraint on the depth extent of the 1788 rupture along the Chirikof and Kodiak segments, but the 3–10 m

tsunami at Sitkinak and at a Russian settlement at Three Saints Bay on the Pacific coast of southwestern Kodiak Island (Lander, 1996) with some down-drop along the Kodiak coast to the northeast (Shennan et al., 2014), suggests much larger, and possibly shallower slip than the 1938 event, which produced no uplift or tsunami inundation on Sitkinak Island (Briggs et al., 2014). Shallow slip near the trench may not have occurred along the southwest half of Kodiak Island in the 1964 rupture (e.g., Johnson et al., 1996; Suito & Freymueller, 2009; Suleimani & Freymueller, 2020), although the estimated slip in the Kodiak asperity seaward of Kodiak varies (e.g., Ichinose et al., 2007). Thus, the extent of any shallow slip overlap of 1788 and 1964 is uncertain, but the 1788 rupture likely extended northeast of the 1938 rupture with larger slip at shallow depth to near Three Saints Bay. In the 150 years between these events, 9 m of slip deficit could have accumulated, only a small fraction (~1 m) of what was released at shallow depth in the 1938 event. Either the coupling is actually much lower than has been estimated (e.g., Wang et al., 2024), or there is significant slip deficit that could generate another event in the 1788 source region.

Data Availability Statement

The bathymetry of North Pacific and U.S. Westcoast are based on the GEBCO grided global bathymetry data (GEBCO Compilation Group, 2023). The bathymetry of Unalaska, Sitka, Crescent City, San Francisco, Santa Monica, San Diego, and Honolulu can be downloaded from NOAA National Geophysical Data Center (2010a, 2010b, 2010c, 2011a, 2011b, 2012a, 2012b). The marigram of the Unalaska can be downloaded from Bai (2025).

Acknowledgments
The work was supported in part by National Natural Science Foundation of China 42376212 (Y. B.), National Key R&D Program of China 2023YFF0803200 (L. Y.), U. S. National Science Foundation Grant EAR1802364 (T. L). We thank the two reviewers, Jeff Freymueller and Shingo Watada, for their constructive comments.

References

Abe, K. (1981). Magnitudes of large shallow earthquakes from 1904 to 1980. *Physics of the Earth and Planetary Interiors*, *27*(1), 72–92. https://doi.org/10.1016/0031-9201(i1)90088-1

Acquisto, T., Bécel, A., Canales, J. P., & Beaucé, E. (2024). Structural controls on megathrust slip behavior inferred from a 3D, crustal-scale, P-wave velocity model of the Alaska Peninsula subduction zone. *Journal of Geophysical Research: Solid Earth*, *129*(11), e2024JB029632. https://doi.org/10.1029/2024JB029632

Allgeyer, S., & Cummins, P. (2014). Numerical tsunami simulation including elastic loading and seawater density stratification. *Geophysical Research Letters*, *41*(7), 2368–2375. https://doi.org/10.1002/2014GL059348

Baba, T., Allgeyer, S., Hossen, J., Cummins, P. R., Tsushima, H., Imai, K., et al. (2017). Accurate numerical simulation of the far-field tsunami caused by the 2011 Tohoku earthquake, including the effects of Boussinesq dispersion, seawater density stratification, elastic loading, and gravitational potential change. *Ocean Modelling*, *111*, 46–54. https://doi.org/10.1016/j.ocemod.2017.01.002

Bai, Y. (2025). Limited shallow slip in the 1938 M_S 8.3 Alaska Peninsula earthquake rupture [Dataset]. https://doi.org/10.5281/zenodo.14586286

Bai, Y., & Cheung, K. F. (2013). Dispersion and nonlinearity of multi-layer non-hydrostatic free-surface flow. *Journal of Fluid Mechanics*, *726*, 226–260. https://doi.org/10.1017/jfm.2013.213

Bai, Y., & Cheung, K. F. (2015). Dispersion and kinematics of multi-layer non-hydrostatic models. *Ocean Modelling*, *92*, 11–27. https://doi.org/10.1016/j.ocemod.2015.05.005

Bai, Y., & Cheung, K. F. (2016). Linear and nonlinear properties of reduced two-layer models for non-hydrostatic free-surface flow. *Ocean Modelling*, *107*, 64–81. https://doi.org/10.1016/j.ocemod.2016.10.003

Bai, Y., & Cheung, K. F. (2018). Linear shoaling of free-surface waves in multi-layer non-hydrostatic models. *Ocean Modelling*, *121*, 90–104. https://doi.org/10.1016/j.ocemod.2017.11.005

Bai, Y., Lay, T., Cheung, K. F., & Ye, L. (2017). Two regions of seafloor deformation generated the tsunami for the 13 November 2016, Kaikoura, New Zealand earthquake. *Geophysical Research Letters*, *44*(13), 6597–6606. https://doi.org/10.1002/2017gl073717

Bai, Y., Liu, C., Lay, T., Cheung, K. F., & Yamazaki, Y. (2023). Fast and slow intraplate ruptures during the 19 October 2020 magnitude 7.6 Shumagin earthquake. *Nature Communications*, *14*(1), 2015. https://doi.org/10.1038/s41467-023-37731-2

Bai, Y., Liu, C., Lay, T., Cheung, K. F., & Ye, L. (2022). Optimizing a model of coseismic rupture for the 22 July 2020 M_W 7.8 Simeonof earthquake by exploiting acute sensitivity of tsunami excitation across the shelf break. *Journal of Geophysical Research: Solid Earth*, *127*(7), e2022JB024484. https://doi.org/10.1029/2022JB024484

Bai, Y., Yamazaki, Y., & Cheung, K. F. (2015a). Interconnection of multi-scale standing waves across the Pacific Basin from the 2011 Tohoku Tsunami. *Ocean Modelling*, *92*, 183–197. https://doi.org/10.1016/j.ocemod.2015.06.007

Bai, Y., Yamazaki, Y., & Cheung, K. F. (2015b). NEOWAVE. In *Proceedings of the 2015 National Tsunami Hazard Mitigation Program Model Benchmarking Workshop* (pp. 165–177). National Weather Service.

Bai, Y., Yamazaki, Y., & Cheung, K. F. (2018). Convergence of multilayer nonhydrostatic models in relation to Boussinesq-type equations. *Journal of Waterway, Port, Coastal, and Ocean Engineering*, *144*(2), 06018001. https://doi.org/10.1061/(ASCE)WW.1943-5460.0000438

Briggs, R. W., Engelhart, S. E., Nelson, A. R., Dura, T., Kemp, A. C., Haeussler, P. J., et al. (2014). Uplift and subsidence reveal a nonpersistent megathrust rupture boundary (Sitkinak Island, Alaska). *Geophysical Research Letters*, *41*(7), 2289–2296. https://doi.org/10.1002/2014GL059380

Brooks, B. A., Goldberg, D., DeSanto, J., Ericksen, T. L., Webb, S. C., Nooner, S. L., et al. (2023). Rapid shallow megathrust afterslip from the 2021 *M* 8.2 Chignik, Alaska earthquake revealed by seafloor geodesy. *Science Advances*, *9*(17), eadf9299. https://doi.org/10.1126/sciadv.adf9299

Cheung, K. F., Bai, Y., & Yamazaki, Y. (2013). Surges around the Hawaiian Islands from the 2011 Tohoku tsunami. *Journal of Geophysical Research: Oceans*, *118*(10), 5703–5719. https://doi.org/10.1002/jgrc.20413

DeMets, C., Gordon, R. G., & Argus, D. F. (2010). Geologically current plate motions. *Geophysical Journal International*, *181*, 1–80. https://doi.org/10.1111/j.1365-246x.2009.04491.x

Dengler, L., & Uslu, B. (2011). Effects of harbor modifications on Crescent City, California's tsunami vulnerability. *Pure and Applied Geophysics*, *168*(6–7), 1175–1185. https://doi.org/10.1007/s00024-010-0224-8

DeSanto, J. B., Webb, S. C., Nooner, S. L., Schmidt, D. A., Crowell, B. W., Brooks, B. A., et al. (2023). Limited shallow slip for the 2020 Simeonof earthquake, Alaska, constrained by GNSS-Acoustic. *Geophysical Research Letters*, *50*(16), e2023GL105045. https://doi.org/10.1029/2023GL105045

Drooff, C., & Freymueller, J. T. (2021). New constraints on slip deficit on the Aleutian megathrust and inflation at Mt. Veniaminof, Alaska from repeat GPS measurements. *Geophysical Research Letters*, *48*(4), e2020GL091787. https://doi.org/10.1029/2020GL091787

Estabrook, C. H., Jacob, K. H., & Sykes, L. R. (1994). Body wave and surface wave analysis of large and great earthquakes along the Eastern Aleutian arc, 1923–1993: Implications for future events. *Journal of Geophysical Research*, *99*(B6), 11643–11662. https://doi.org/10.1029/93jb03124

Freymueller, J. T., Suleimani, E. N., & Nicolsky, D. J. (2021). Constraints on the slip distribution of the 1938 M_W 8.3 Alaska Peninsula earthquake from tsunami modeling. *Geophysical Research Letters*, *48*(9), e2021GL092812. https://doi.org/10.1029/2021GL092812

Fujii, Y., Satake, K., Watada, S., & Ho, T.-C. (2021). Re-examination of slip distribution of the 2004 Sumatra-Andaman earthquake (M_W 9.2) by the inversion of tsunami data using green's functions corrected for compressible seawater over the elastic earth. *Pure and Applied Geophysics*, *178*(12), 4777–4796. https://doi.org/10.1007/s00024-021-02909-6

GEBCO Compilation Group. (2023). General bathymetric chart of the oceans (GEBCO) 2023 grid [Dataset]. Retrieved from https://www.gebco.net/data_and_products/gridded_bathymetry_data/

Gutenberg, B., & Richter, C. F. (1949). *Seismicity of the Earth and Associated phenomena* (p. 267). Princeton University Press.

Hartzell, S. H., & Heaton, T. H. (1985). Teleseismic time functions for large, shallow subduction zone earthquakes. *Bulletin of the Seismological Society of America*, *75*, 965–1004.

He, B., Wei, X. Z., Wei, M., Shen, Y., Alvarez, M., & Schwartz, S. Y. (2023). A shallow slow slip event in 2018 in the Semidi segment of the Alaska subduction zone detected by machine learning. *Earth and Planetary Science Letters*, *612*, 118154. https://doi.org/10.1016/j.epsl.2023.118154

Hill, E. M., Borrero, J. C., Huang, Z., Qiu, Q., Banerjee, P., Natawidjaja, D. H., et al. (2012). The 2010 M_W 7.8 Mentawai earthquake: Very shallow source of a rare tsunami earthquake determined from tsunami field survey and near-field GPS data. *Journal of Geophysical Research*, *117*(B6). https://doi.org/10.1029/2012jb009159

Ichinose, G., Somerville, P., Thio, H. K., Graves, R., & O'Connell, D. (2007). Rupture process of the 1964 Prince William Sound, Alaska, earthquake from the combined inversion of seismic, tsunami, and geodetic data. *Journal of Geophysical Research*, *112*(B7), B07306. https://doi.org/10.1029/2006JB004728

Johnson, J. M., & Satake, K. (1994). Rupture extent of the 1938 Alaskan earthquake as inferred from tsunami waveforms. *Geophysical Research Letters*, *21*(8), 733–736. https://doi.org/10.1029/94gl00333

Johnson, J. M., Satake, K., Holdahl, S. R., & Sauber, J. (1996). The 1964 Prince William Sound earthquake: Joint inversion of tsunami waveforms and geodetic data. *Journal of Geophysical Research*, *101*(B1), 523–532. https://doi.org/10.1029/95jb02806

Kanamori, H. (1972). Mechanism of tsunami earthquakes. *Physics of the Earth and Planetary Interiors*, *6*(5), 346–359. https://doi.org/10.1016/0031-9201(72)90058-1

Kanamori, H. (2014). The diversity of large earthquakes and its implications for hazard mitigation. *Annual Review of Earth and Planetary Sciences*, *42*(1), 7–26. https://doi.org/10.1146/annurev-earth-060313-055034

Lander, J. F. (1996). *Tsunamis affecting Alaska 1737-1996* Documentation No. 31 (p. 205). National Geophysical Data Center.

Lay, T., Ammon, C. J., Kanamori, H., Yamazaki, Y., Cheung, K. F., & Hutko, A. R. (2011). The 25 October 2010 Mentawai tsunami earthquake (M_W 7.8) and the tsunami hazard presented by shallow megathrust ruptures. *Geophysical Research Letters*, *38*(6), L13301. https://doi.org/10.1029/2010gl046552

Lay, T., & Bilek, S. (2007). Anomalous earthquake ruptures at shallow depths on subduction zone megathrusts. In *The seismogenic zone of subduction thrust faults* (pp. 476–511). Columbia University Press.

Lay, T., Kanamori, H., Ammon, C. J., Koper, K. D., Hutko, A. R., Ye, L., et al. (2012). Depth-varying rupture properties of subduction zone megathrust faults. *Journal of Geophysical Research*, *117*(B4), B04311. https://doi.org/10.1029/2011JB009133

Lay, T., Ye, L., Kanamori, H., Yamazaki, Y., Cheung, K. F., Kwong, K., & Koper, K. D. (2013). The October 28, 2012 M_W 7.8 Haida Gwaii underthrusting earthquake and tsunami: Slip partitioning along the Queen Charlotte Fault transpressional plate boundary. *Earth and Planetary Science Letters*, *375*, 57–70. https://doi.org/10.1016/j.epsl.2013.05.005

Li, L., & Cheung, K. F. (2019). Numerical dispersion in non-hydrostatic modeling of long-wave propagation. *Ocean Modelling*, *138*, 68–87. https://doi.org/10.1016/j.ocemod.2019.05.002

Li, L., Cheung, K. F., Yue, H., Lay, T., & Bai, Y. (2016). Effects of dispersion in tsunami Green's functions and implications for joint inversion with seismic and geodetic data: A case study of the 2010 Mentawai M_W 7.8 earthquake. *Geophysical Research Letters*, *43*(21), 11–182. https://doi.org/10.1002/2016gl070970

Li, L., Lay, T., Cheung, K. F., & Ye, L. (2016). Joint modeling of teleseismic and tsunami wave observations to constrain the 16 September 2015 Illapel, Chile, M_W 8.3 earthquake rupture process. *Geophysical Research Letters*, *43*(9), 4303–4312. https://doi.org/10.1002/2016gl068674

Li, S., & Freymueller, J. T. (2018). Spatial variation of slip behavior beneath the Alaska Peninsula along Alasak-Aleutian subduction zone. *Geophysical Research Letters*, *45*(8), 3453–3460. https://doi.org/10.1002/2017GL076761

Liu, C., Bai, Y., Lay, T., Feng, Y., & Xiong, X. (2023). Megathrust complexity and the up-dip extent of slip during the 2021 Chignik, Alaska Peninsula earthquake. *Tectonophysics*, *854*, 229808. https://doi.org/10.1016/j.tecto.2023.229808

Liu, C., Bai, Y., Lay, T., He, P., Wen, Y., Wei, X., et al. (2024). Shallow crustal rupture in a major M_W 7.5 earthquake above a deep crustal seismic swarm along the Noto Peninsula in western Japan. *Earth and Planetary Science Letters*, *648*, 119107. https://doi.org/10.1016/j.epsl.2024.119107

Mulia, I. E., Gusman, A. R., Heidarzadeh, M., & Satake, K. (2022). Sensitivity of tsunami data to the up-dip extent of the July 2021 M_W 8.2 Alaska earthquake. *Seismological Research Letters*, *93*(4), 1992–2003. https://doi.org/10.1785/0220210359

Mulia, I. E., Heidarzadeh, M., & Satake, K. (2022). Effects of depth of fault slip and continental shelf geometry on the generation of anomalously long-period tsunami by the July 2020 M_W 7.8 Shumagin (Alaska) earthquake. *Geophysical Research Letters*, *49*(3), e2021GL094937. https://doi.org/10.1029/2021GL094937

Nelson, A. R., Briggs, R. W., Dura, T., Engelhart, S. E., Gelenbaum, G., Bradley, L.-A., et al. (2015). Tsunami recurrence in the eastern Alaska-Aleutian arc: A Holocene stratigraphic record from Chirikof Island, Alaska. *Geosphere*, *11*(4), 1172–1203. https://doi.org/10.1130/GES01108.1

Neumann, F. (1940). *United States earthquakes, 1938*. U.S. Coast and Geodetic Survey.

NOAA National Geophysical Data Center. (2010a). Crescent City, California 1/3 arc-second NAVD 88 Coastal Digital Elevation Model [Dataset]. *NOAA National Centers for Environmental Information*. Retrieved from https://www.ncei.noaa.gov/metadata/geoportal/rest/metadata/item/gov.noaa.ngdc.mgg.dem:724/html

NOAA National Geophysical Data Center. (2010b). San Francisco Bay, California 1/3 arc-second NAVD 88 Coastal Digital Elevation Model [Dataset]. *NOAA National Centers for Environmental Information*. Retrieved from https://www.ncei.noaa.gov/metadata/geoportal/rest/metadata/item/gov.noaa.ngdc.mgg.dem:741/html

NOAA National Geophysical Data Center. (2010c). Santa Monica, California 1/3 arc-second NAVD 88 Coastal Digital Elevation Model [Dataset]. *NOAA National Centers for Environmental Information*. Retrieved from https://www.ncei.noaa.gov/metadata/geoportal/rest/metadata/item/gov.noaa.ngdc.mgg.dem:726/html

NOAA National Geophysical Data Center. (2011a). Oahu, Hawaii 1/3 arc-second MHW Coastal Digital Elevation Model [Dataset]. *NOAA National Centers for Environmental Information*. Retrieved from https://www.ncei.noaa.gov/metadata/geoportal/rest/metadata/item/gov.noaa.ngdc.mgg.dem:3410/html

NOAA National Geophysical Data Center. (2011b). Sitka, Alaska 1/3 arc-second MHW Coastal Digital Elevation Model [Dataset]. *NOAA National Centers for Environmental Information*. Retrieved from https://www.ncei.noaa.gov/metadata/geoportal/rest/metadata/item/gov.noaa.ngdc.mgg.dem:1844/html

NOAA National Geophysical Data Center. (2012a). San Diego, California 1/3 Arc-second NAVD 88 Coastal Digital Elevation Model [Dataset]. *NOAA National Centers for Environmental Information*. Retrieved from https://www.ncei.noaa.gov/metadata/geoportal/rest/metadata/item/gov.noaa.ngdc.mgg.dem:3542/html

NOAA National Geophysical Data Center. (2012b). Unalaska, Alaska 8/15 arc-second MHHW Coastal Digital Elevation Model [Dataset]. *NOAA National Centers for Environmental Information*. Retrieved from https://www.ncei.noaa.gov/access/metadata/landingpage/bin/iso?id=gov.noaa.ngdc.mgg.dem:4270

Shennan, I., Barlow, N., Carver, G., Davies, F., Garrett, E., & Hocking, E. (2014). Great tsunamigenic earthquakes during the past 1000 yr on the Alaska megathrust. *Geology*, *42*(8), 687–690. https://doi.org/10.1130/G35797.1

Shillington, D. J., Bécel, A., & Nedimovic, M. R. (2022). Upper plate structure and megathrust properties in the Shumagin gap near the July 2020 *M*7.8 Simeon of event. *Geophysical Research Letters*, *49*(2), 32021GL096974. https://doi.org/10.1029/2021GL096974

Suito, H., & Freymueller, J. T. (2009). A viscoelastic and afterslip postseismic deformation model for the 1964 Alaska earthquake. *Journal of Geophysical Research*, *114*(B11), B11404. https://doi.org/10.1029/2008JB005954

Suleimani, E., & Freymueller, J. T. (2020). Near-field modeling of the 1964 Alaska tsunami: The role of splay faults and horizontal displacements. *Journal of Geophysical Research: Solid Earth*, *125*(7), e2020JB019620. https://doi.org/10.1029/2020JB019620

Sykes, L. R. (1971). Aftershock zones of great earthquakes, seismicity gaps, and earthquake prediction for Alaska and the Aleutians. *Journal of Geophysical Research*, *76*(32), 8021–8041. https://doi.org/10.1029/jb076i032p08021

Sykes, L. R., Kisslinger, J. B., House, L., Davies, J. N., & Jacob, K. H. (1981). Rupture zones and repeat times of great earthquakes along the Alaska–Aleutian arc, 1784–1980. In D. W. Simpson & P. G. Richards (Eds.), *Earthquake prediction: An international review* (Vol. 4, pp. 73–80). American Geophysical Union. https://doi.org/10.1029/me004p0073

Tape, C., & Lomax, A. (2022). Aftershock regions of Aleutian-Alaska megathrust earthquakes, 1938–2021. *Journal of Geophysical Research: Solid Earth*, *127*(7), e2022JB024336. https://doi.org/10.1029/2022JB024336

Tsai, V. C., Ampuero, J.-P., Kanamori, H., & Stevenson, D. J. (2013). Estimating the effect of Earth elasticity and variable water density on tsunami speeds. *Geophysical Research Letters*, *40*(3), 492–496. https://doi.org/10.1002/grl.50147

Wang, F., Wei, S. S., Drooff, C., Elliott, J. L., Freymueller, J. T., Ruppert, N. A., & Zhang, H. (2024). Fluids control along-strike variations in the Alaska megathrust slip. *Earth and Planetary Science Letters*, *633*, 118655. https://doi.org/10.1016/j.epsl.2024.118655

Watada, S. (2023). Progress and application of the synthesis of trans-oceanic tsunamis. *Progress in Earth and Planetary Science*, *10*(1), 26. https://doi.org/10.1186/s40645-023-00555-1

Watada, S., Kusumoto, S., & Satake, K. (2014). Traveltime delay and initial phase reversal of distant tsunamis coupled with the self-gravitating elastic Earth. *Journal of Geophysical Research: Solid Earth*, *119*(5), 4287–4310. https://doi.org/10.1002/2013JB010841

Wei, X., Zhi, H., & Bai, Y. (2024). Multi-layer non-hydrostatic free-surface flow model with kinematic seafloor for seismic tsunami generation. *Coastal Engineering*, *193*, 104580. https://doi.org/10.1016/j.coastaleng.2024.104580

Witter, R. C., Briggs, R. W., Engelhart, S. E., Gelfenbaum, G., Koehler, R. D., & Barnhart, W. D. (2014). Little late Holocene strain accumulation and release on the Aleutian megathrust below the Shumagin Islands, Alaska. *Geophysical Research Letters*, *41*(7), 2359–2367. https://doi.org/10.1002/2014GL059393

Xia, T., Ye, L., Bai, Y., Lay, T., Xu, S., Kanamori, H., et al. (2024). The 2022 M_W 7.3 southern Sumatra tsunami Earthquake: Rupture up-dip of the 2007 M_W 8.4 Bengkulu event. *Journal of Geophysical Research: Solid Earth*, *129*(12), e2024JB030284. https://doi.org/10.1029/2024jb030284

Xiao, Z., Freymueller, J. T., Grapenthin, R., Elliott, J. L., Drooff, C., & Fusso, L. (2021). The deep Shumagin gap filled: Kinematic rupture model and slip budget analysis of the 2020 M_W 7.8 Simeonof earthquake constrained by GNSS, global seismic waveforms, and floating InSAR. *Earth and Planetary Science Letters*, *576*, 117241. https://doi.org/10.1016/j.epsl.2021.117241

Yamazaki, Y., Bai, Y., Goo, L. L., Cheung, K. F., & Lay, T. (2023). Nonhydrostatic modeling of tsunamis from earthquake rupture to coastal impact. *Journal of Hydraulic Engineering*, *149*(9), 04023033. https://doi.org/10.1061/jhend8.hyeng-13388

Yamazaki, Y., Cheung, K. F., & Kowalik, Z. (2011). Depth-integrated, non-hydrostatic model with grid nesting for tsunami generation, propagation, and run-up. *International Journal for Numerical Methods in Fluids*, *67*(12), 2081–2107. https://doi.org/10.1002/fld.2485

Yamazaki, Y., Cheung, K. F., Kowalik, Z., Lay, T., & Pawlak, G. (2012). NEOWAVE. In *Proceedings of the NTHMP Model Benchmarking Workshop* (pp. 239–302). National Weather Service.

Yamazaki, Y., Cheung, K. F., & Lay, T. (2018). A self-consistent fault slip model for the 2011 Tohoku earthquake and tsunami. *Journal of Geophysical Research: Solid Earth*, *123*(2), 1435–1458. https://doi.org/10.1002/2017jb014749

Yamazaki, Y., Kowalik, Z., & Cheung, K. F. (2009). Depth-integrated, non-hydrostatic model for wave breaking and run-up. *International Journal for Numerical Methods in Fluids*, *61*(5), 473–497. https://doi.org/10.1002/fld.1952

Yamazaki, Y., Lay, T., & Cheung, K. F. (2021). A compound faulting model for the 1975 Kalapana, Hawaii, earthquake, landslide, and tsunami. *Journal of Geophysical Research: Solid Earth*, *126*(11), e2021JB022488. https://doi.org/10.1029/2021jb022488

Yamazaki, Y., Lay, T., Cheung, K. F., Witter, R. C., La Selle, S. M., & Jaffe, B. E. (2024). A great tsunami earthquake component of the 1957 Aleutian Islands earthquake. *Earth and Planetary Science Letters*, *637*, 118691. https://doi.org/10.1016/j.epsl.2024.118691

Yamazaki, Y., Lay, T., Cheung, K. F., Yue, H., & Kanamori, H. (2011). Modeling near-field tsunami observations to improve finite-fault slip models for the 11 March 2011 Tohoku earthquake. *Geophysical Research Letters*, *38*(7). https://doi.org/10.1029/2011gl049130

Ye, L., Bai, Y., Si, D., Lay, T., Cheung, K. F., & Kanamori, H. (2022). Rupture model for the 29 July 2021 M_W 8.2 Chignik, Alaska earthquake constrained by seismic, geodetic, and tsunami observations. *Journal of Geophysical Research: Solid Earth*, *127*(7), e2021JB023676. https://doi.org/10.1029/2021JB023676

Ye, L., Lay, T., Kanamori, H., Yamazaki, Y., & Cheung, K. F. (2021). The 22 July 2020 *Mw* 7.8 Shumagin seismic gap earthquake: Partial rupture of a weakly coupled megathrust. *Earth and Planetary Science Letters*, *562*, 116879. https://doi.org/10.1016/j.epsl.2021.116879

Yue, H., Lay, T., Rivera, L., Bai, Y., Yamazaki, Y., Cheung, K. F., et al. (2014). Rupture process of the 2010 M_W 7.8 Mentawai tsunami earthquake from joint inversion of near-field hr-GPS and teleseismic body wave recordings constrained by tsunami observations. *Journal of Geophysical Research: Solid Earth*, *119*(7), 5574–5593. https://doi.org/10.1002/2014jb011082

Zhao, B., Bürgmann, R., Wang, D., Zhang, J., Yu, J., & Li, Q. (2022). Aseismic slip and recent ruptures of persistent asperities along the Alaska-Aleutian subduction zone. *Nature Communications*, *13*(1), 3098. https://doi.org/10.1038/s41467-022-30883-7

Geophysical Research Letters

Supporting Information for

Limited Shallow Slip in the 1938 M_S 8.3 Alaska Peninsula Earthquake Rupture

Yefei Bai[1,2,*], Honghuan Zhi[1], Thorne Lay[3], Chengli Liu[4], Lingling Ye[5,*], Kwok Fai Cheung[6]

[1]Ocean College, Zhejiang University, Zhoushan, Zhejiang, China
[2]Hainan Institute, Zhejiang University, Sanya, Hainan, China
[3]Department of Earth and Planetary Sciences, University of California, Santa Cruz, CA, USA
[4]School of Geophysics and Geomatics, China University of Geosciences, Wuhan, Hubei, China
[5]Department of Earth and Space Sciences, Southern University of Science and Technology, Shenzhen, China
[6]Department of Ocean and Resources Engineering, University of Hawaii at Manoa, Honolulu, Hawaii, USA

Corresponding author: Yefei Bai (yfbai@zju.edu.cn); Lingling Ye (yell@sustech.edu.cn)

Contents of this file

Figures S1 to S14

Additional Supporting Information (Files uploaded separately)

Captions for Movies S1 to S2.

Introduction

This supporting information includes 14 Figures that provide the detailed bathymetric models and harbor adjustments made for the 1938 tide gauge calculations along with models and predictions relative to the 1938 observations for the 2021 Chignik slip modes of Liu et al. (2023) and Ye et al. (2022), four sensitivity test models and corresponding tide gauge calculations, maps of the maximum sea surface elevation in the near-field and far-field for the preferred models, and two corresponding animations of the sea surface time history for the preferred model.

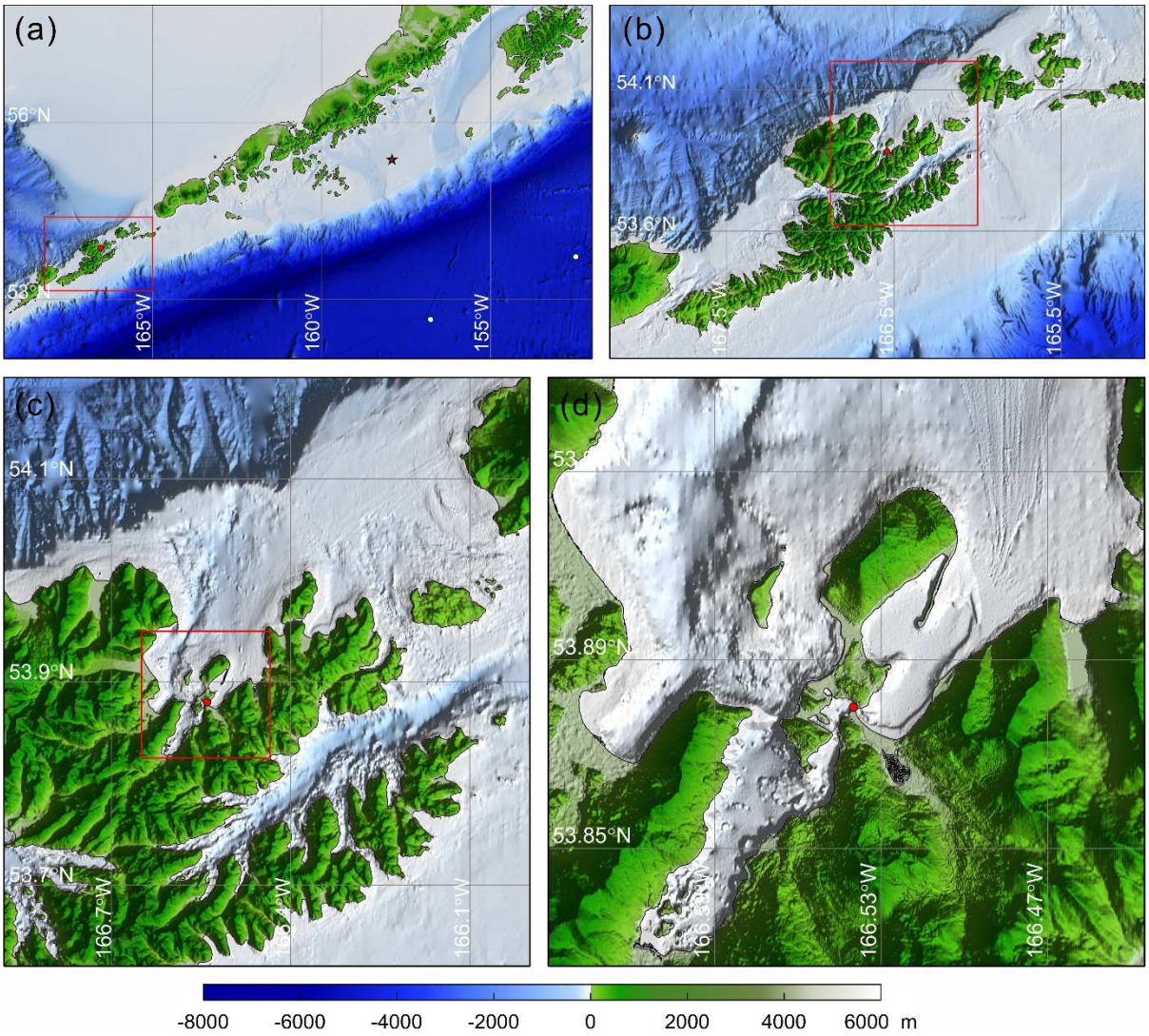

Figure S1. Bathymetry in the level 2 to level 5 nested grids used for the tide gauge calculation at Unalaska. Red star and circle indicate epicenter and tide gauge locations, respectively.

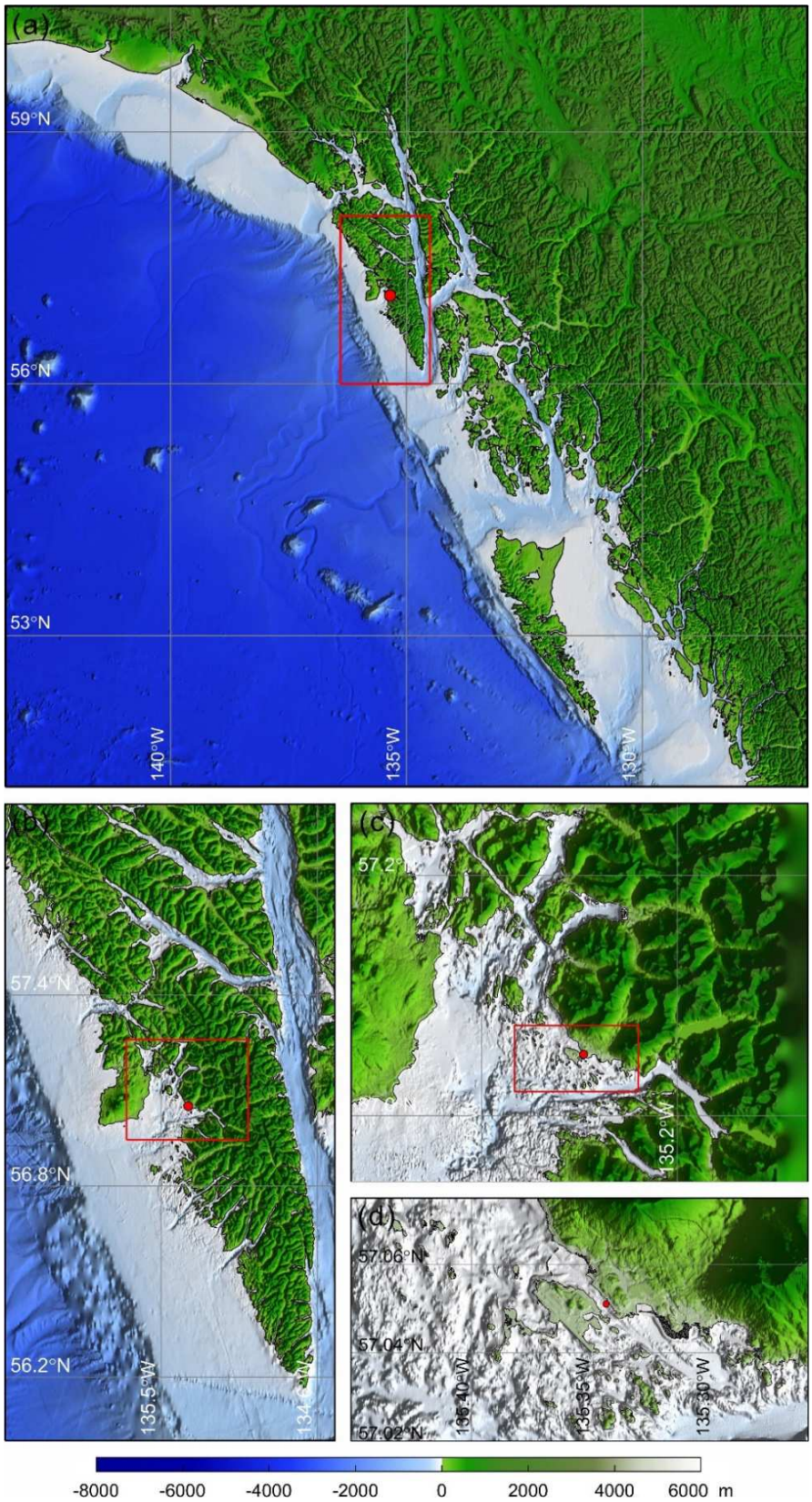

Figure S2. Bathymetry in the level 2 to level 5 nested grids used for the tide gauge calculation at Sitka. Red circle indicates tide gauge location.

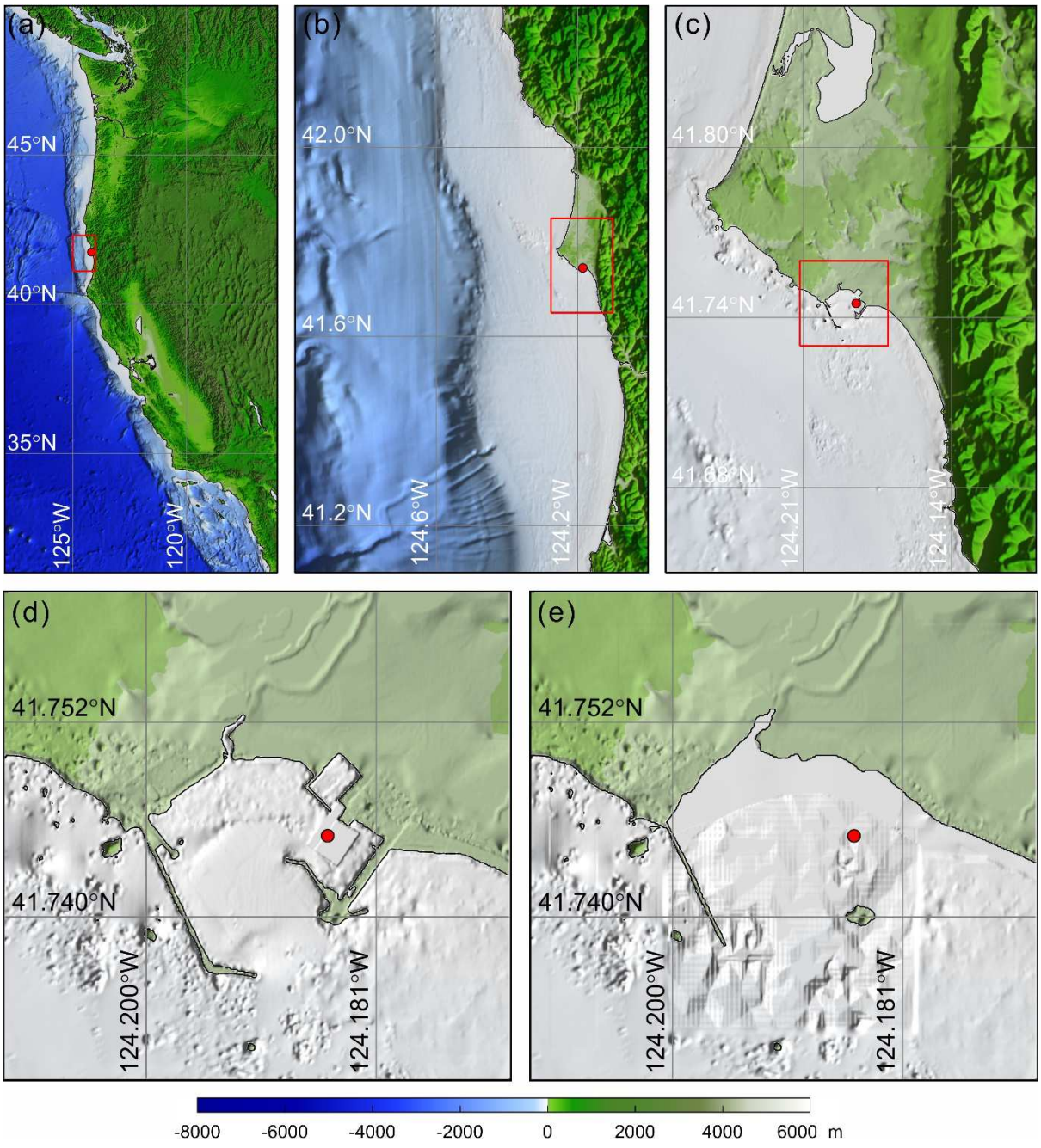

Figure S3. Bathymetry in the level 2 to level 5 nested grids used for the tide gauge calculation at Crescent City. The bottom right image shows the reconstructed harbor design for the 1938 configuration. Red circle indicates tide gauge location.

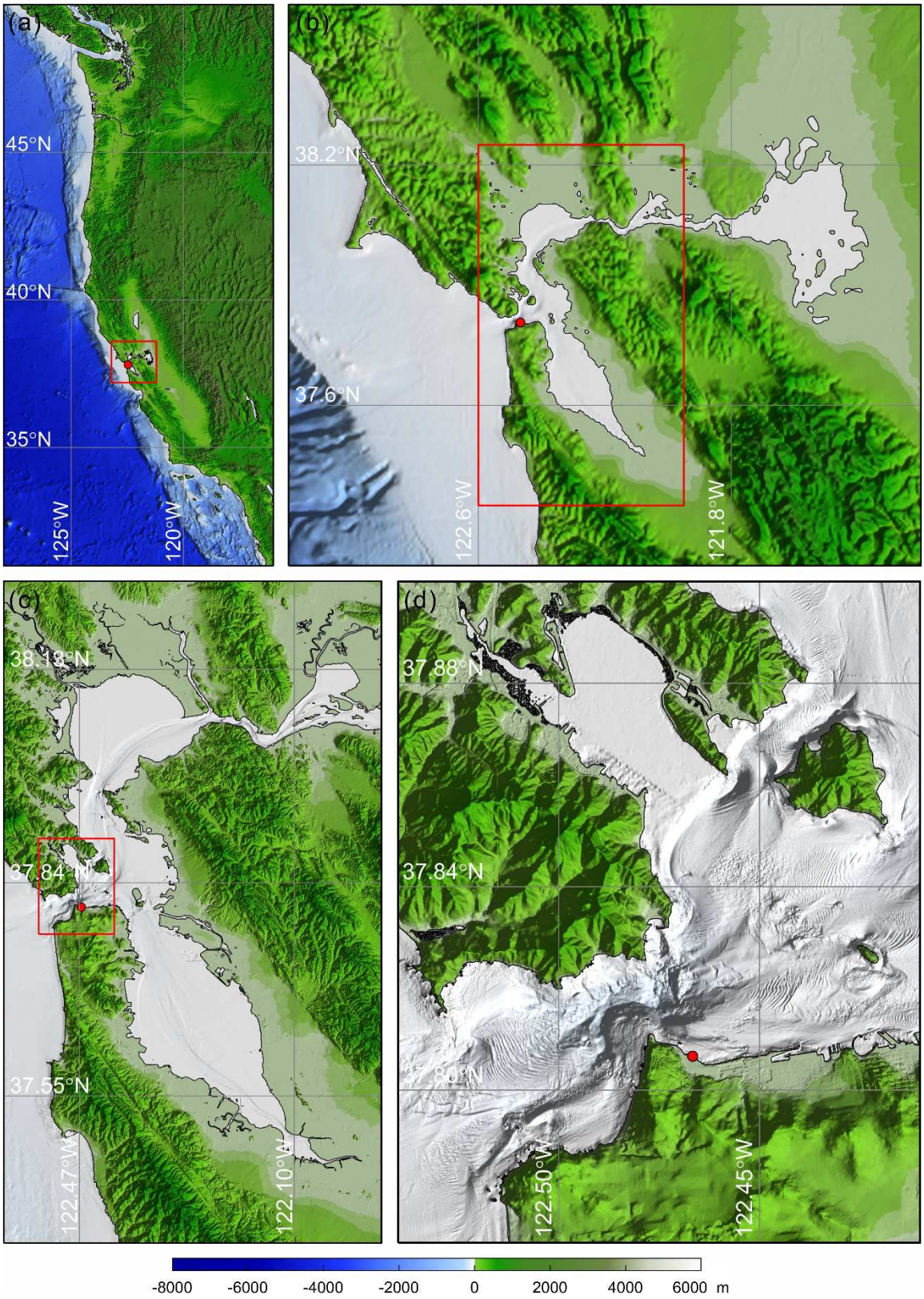

Figure S4. Bathymetry in the level 2 to level 5 nested grids used for the tide gauge calculation at San Francisco. Red circle indicates tide gauge location.

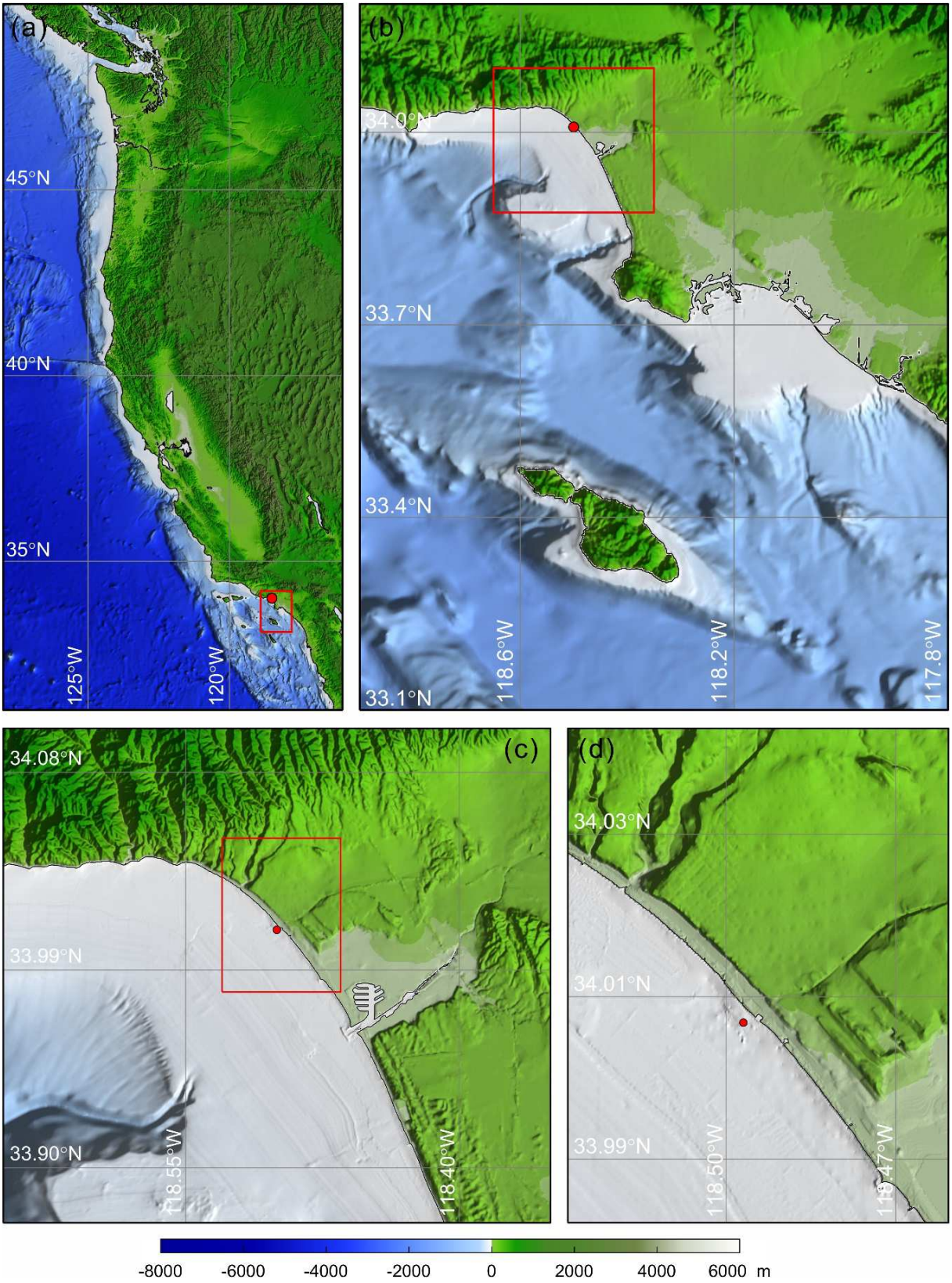

Figure S5. Bathymetry in the level 2 to level 5 nested grids used for the tide gauge calculation at Santa Monica. Red circle indicates tide gauge location.

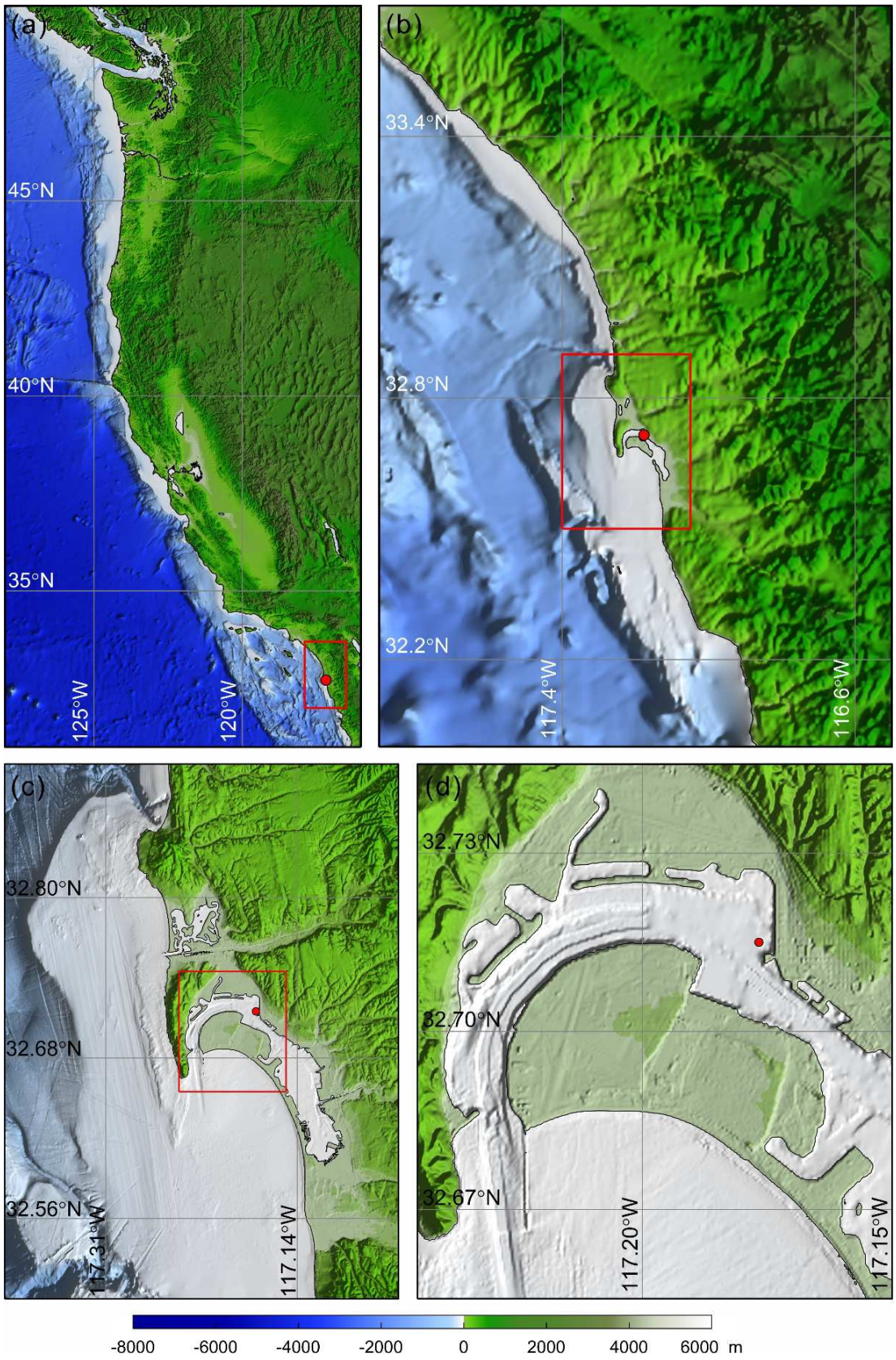

Figure S6. Bathymetry in the level 2 to level 5 nested grids used for the tide gauge calculation at San Diego. Red circle indicates tide gauge location.

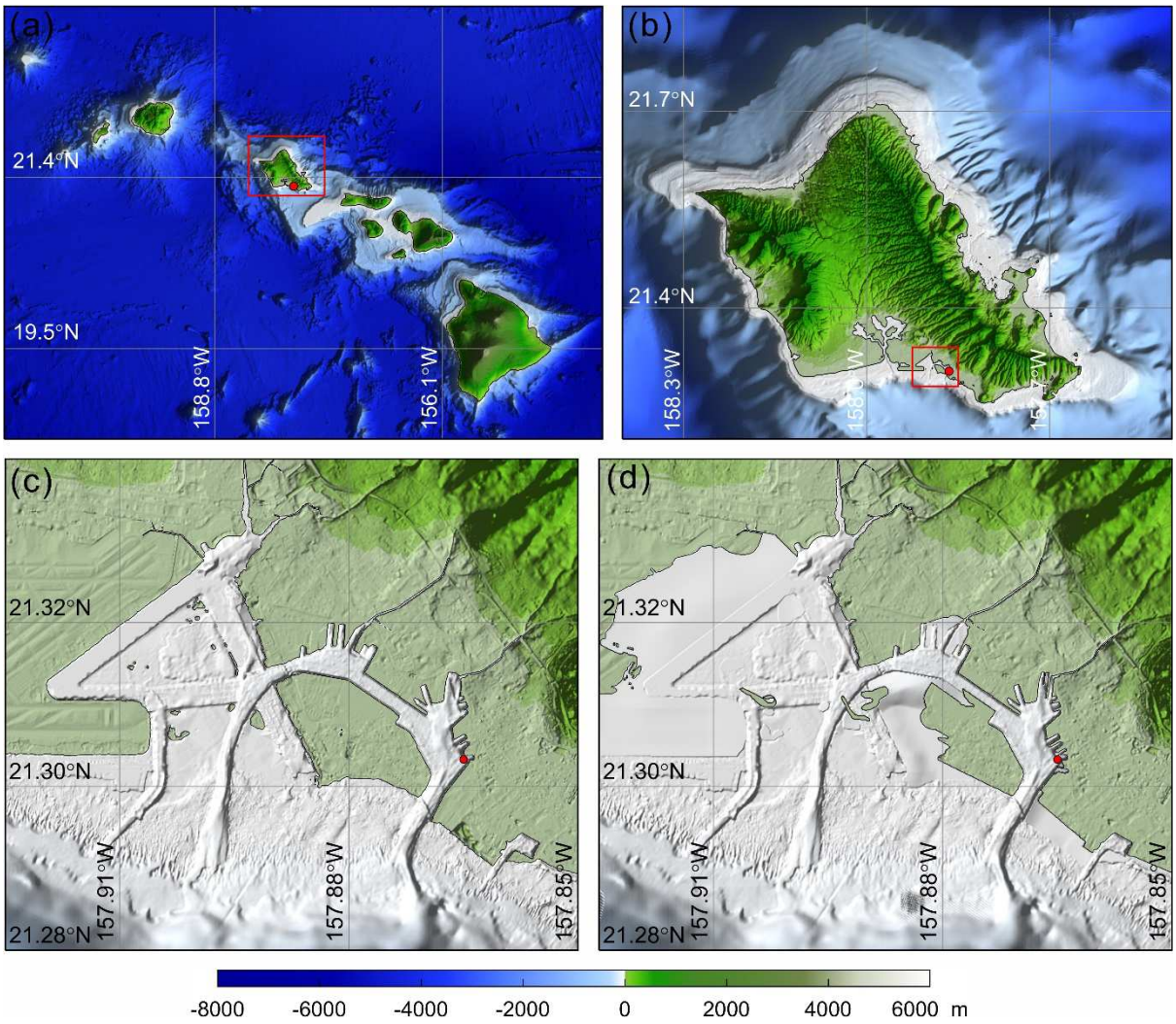

Figure S7 Bathymetry in the level 2 to level 4 nested grids used for the tide gauge calculation at Honolulu. The bottom right image shows the reconstructed harbor design for the 1938 configuration. Red circle indicates tide gauge location.

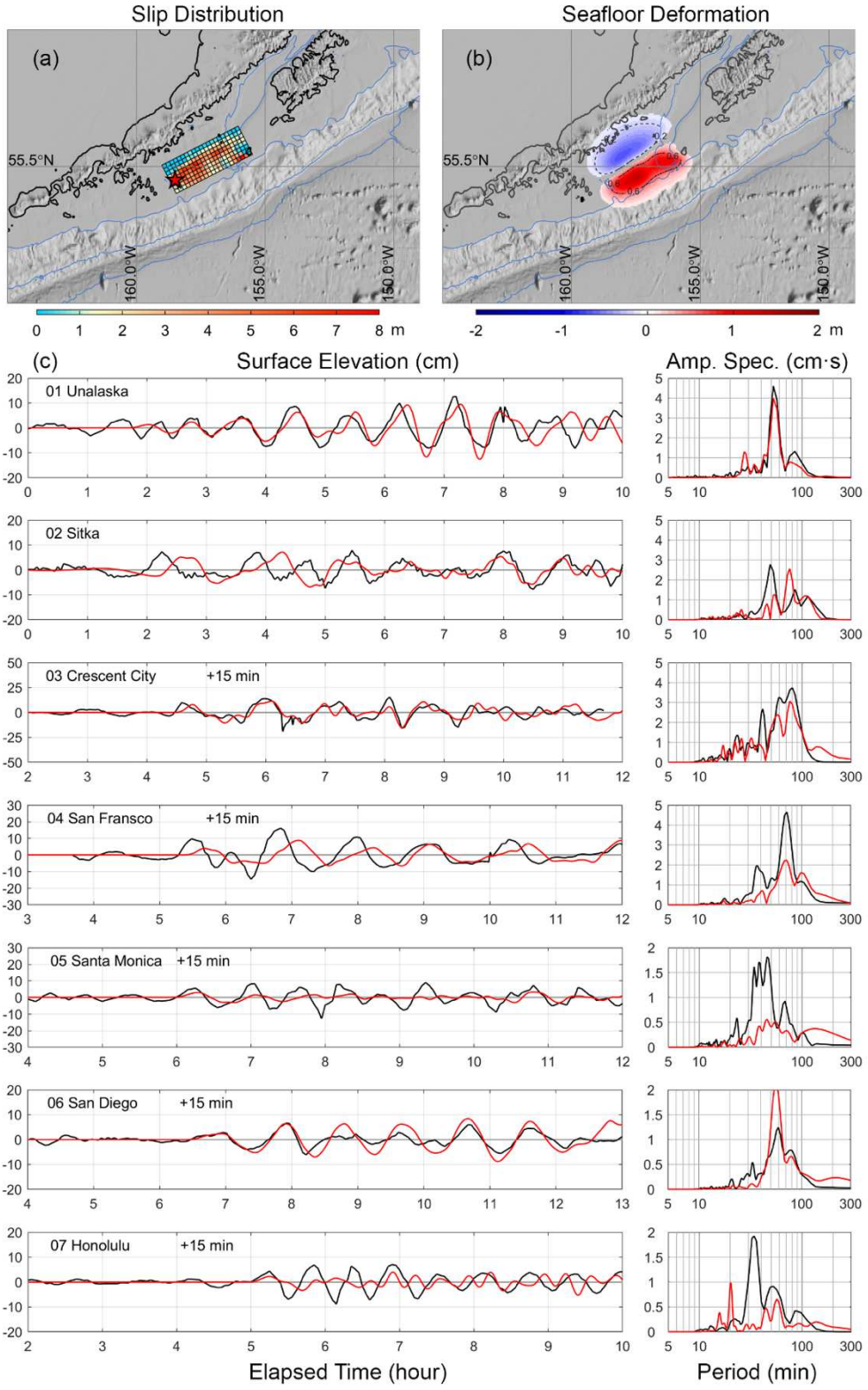

Figure S8. (a) The slip model for the 2021 M_W 8.2 Chignik earthquake from Liu et al. (2023), **(b)** corresponding seafloor deformation, and **(c)** comparison of 1938 observed tsunami tide gauge recordings and spectra (black lines) and tsunami calculations for the 2021 model (red lines).

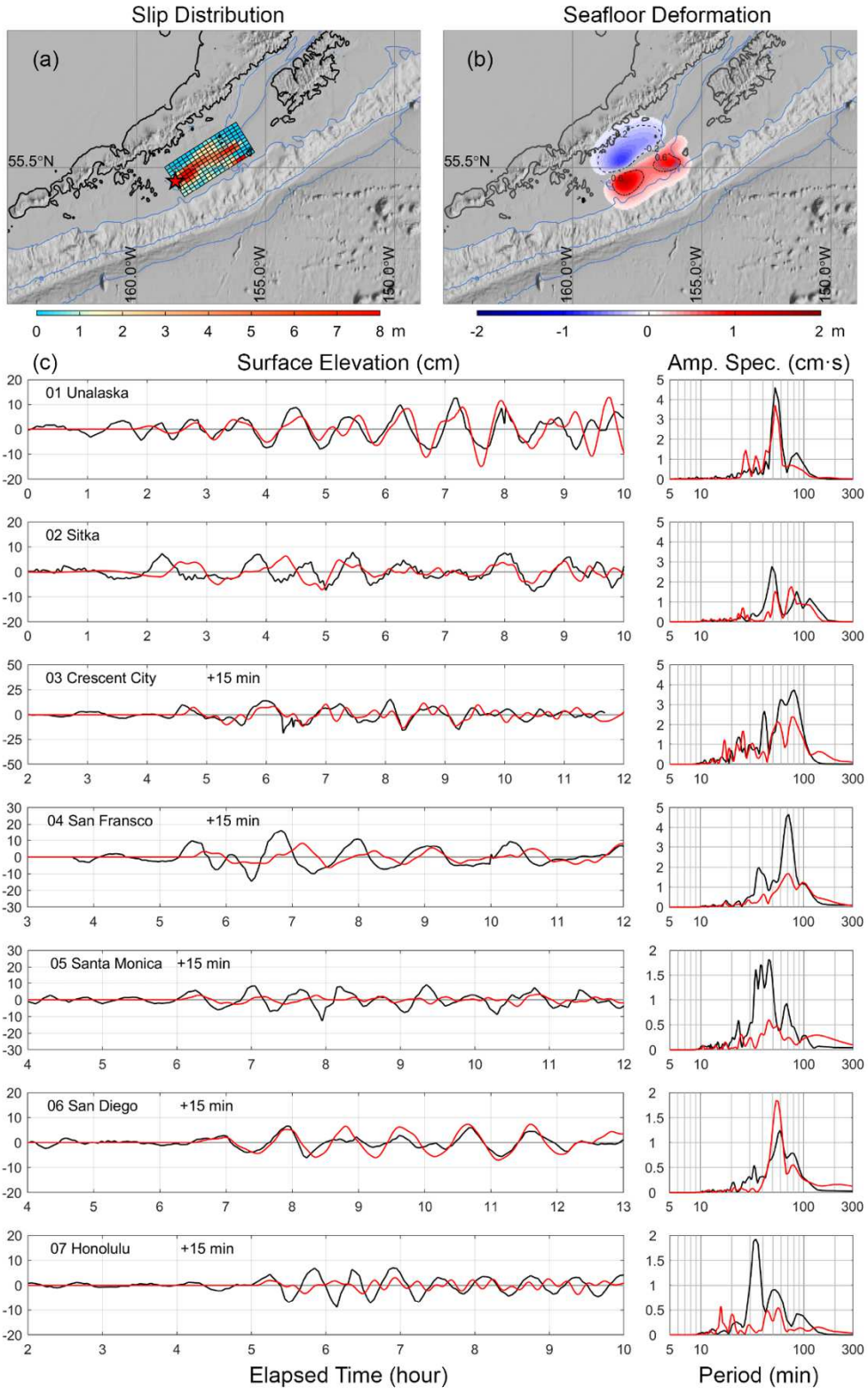

Figure S9. (a) The slip model for the 2021 *Mw* 8.2 Chignik earthquake from Ye et al. (2022), **(b)** corresponding seafloor deformation, and **(c)** comparison of 1938 observed tsunami tide gauge recordings and spectra (black lines) and tsunami calculations for the 2021 model (red lines).

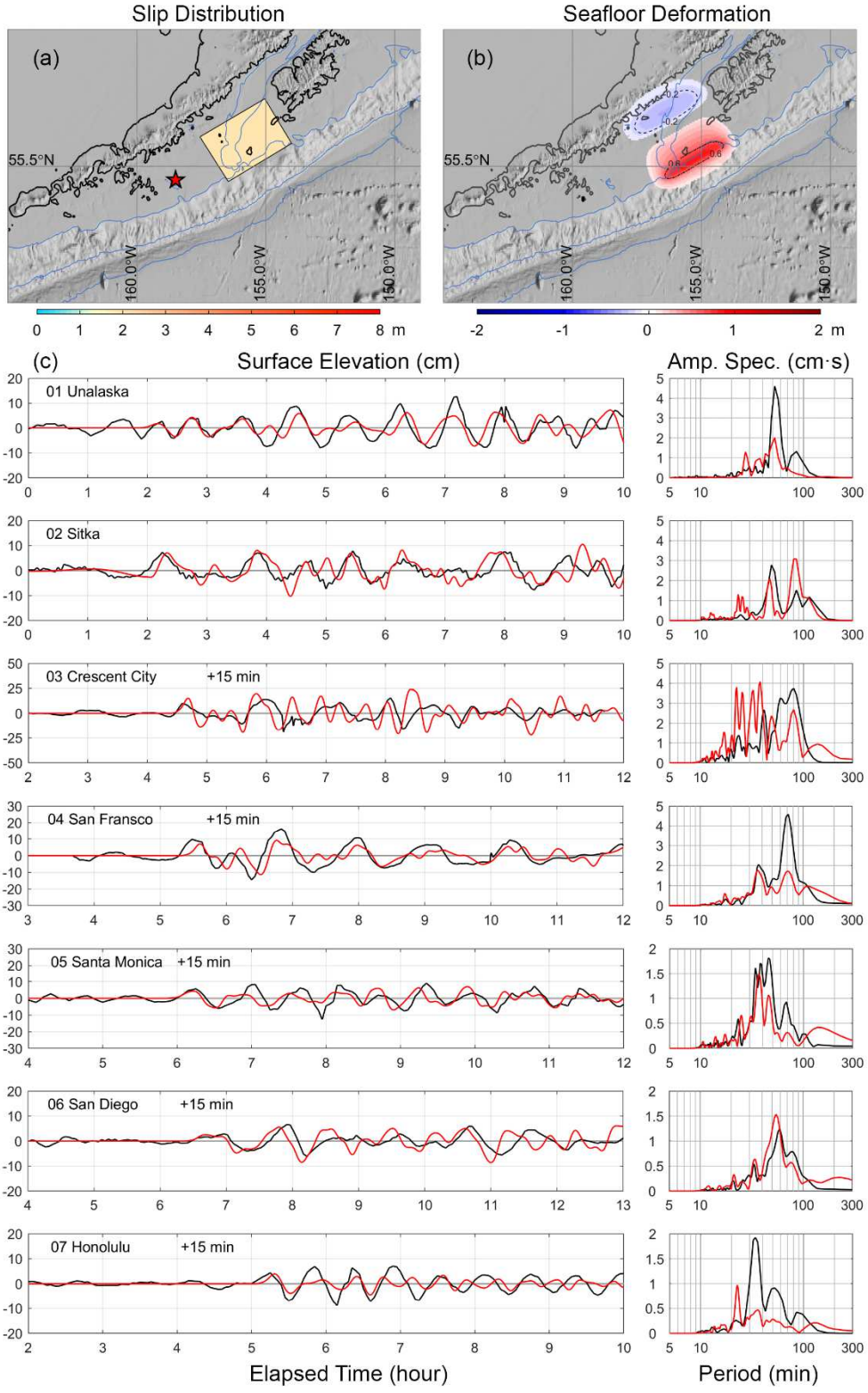

Figure S10. (a) The test model 1 with only 2-m deep slip for the sensitivity of the preferred model in the study, **(b)** corresponding seafloor deformation, and **(c)** comparison of 1938 observed tsunami tide gauge recordings and spectra (black lines) and tsunami calculations for the test model 1 (red lines).

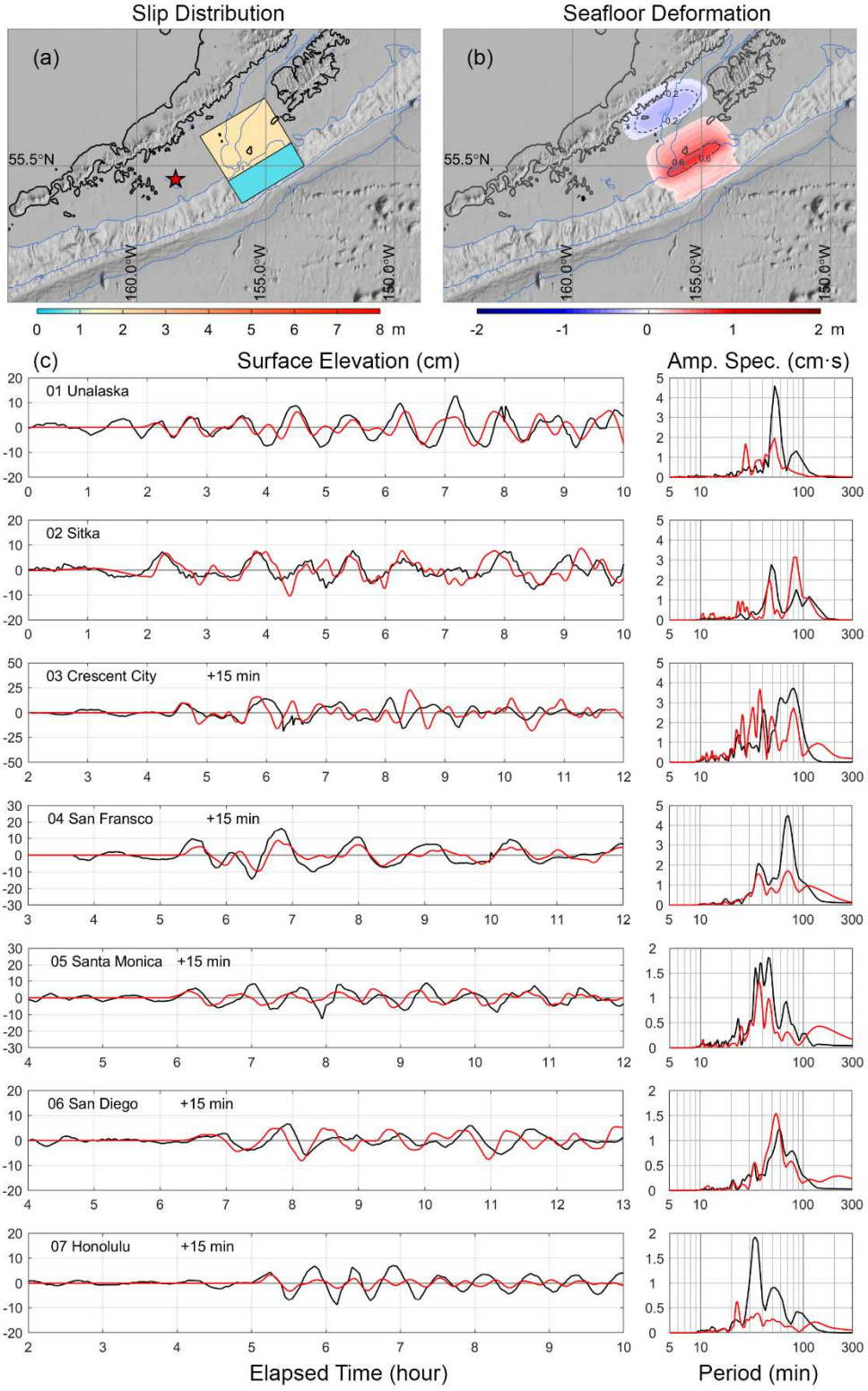

Figure S11. (a) The test model 2 with only 2-m deep slip and 0.5m-shallow slip for the sensitivity of the preferred model in the study, **(b)** corresponding seafloor deformation, and **(c)** comparison of 1938 observed tsunami tide gauge recordings and spectra (black lines) and tsunami calculations for the test model 2 (red lines).

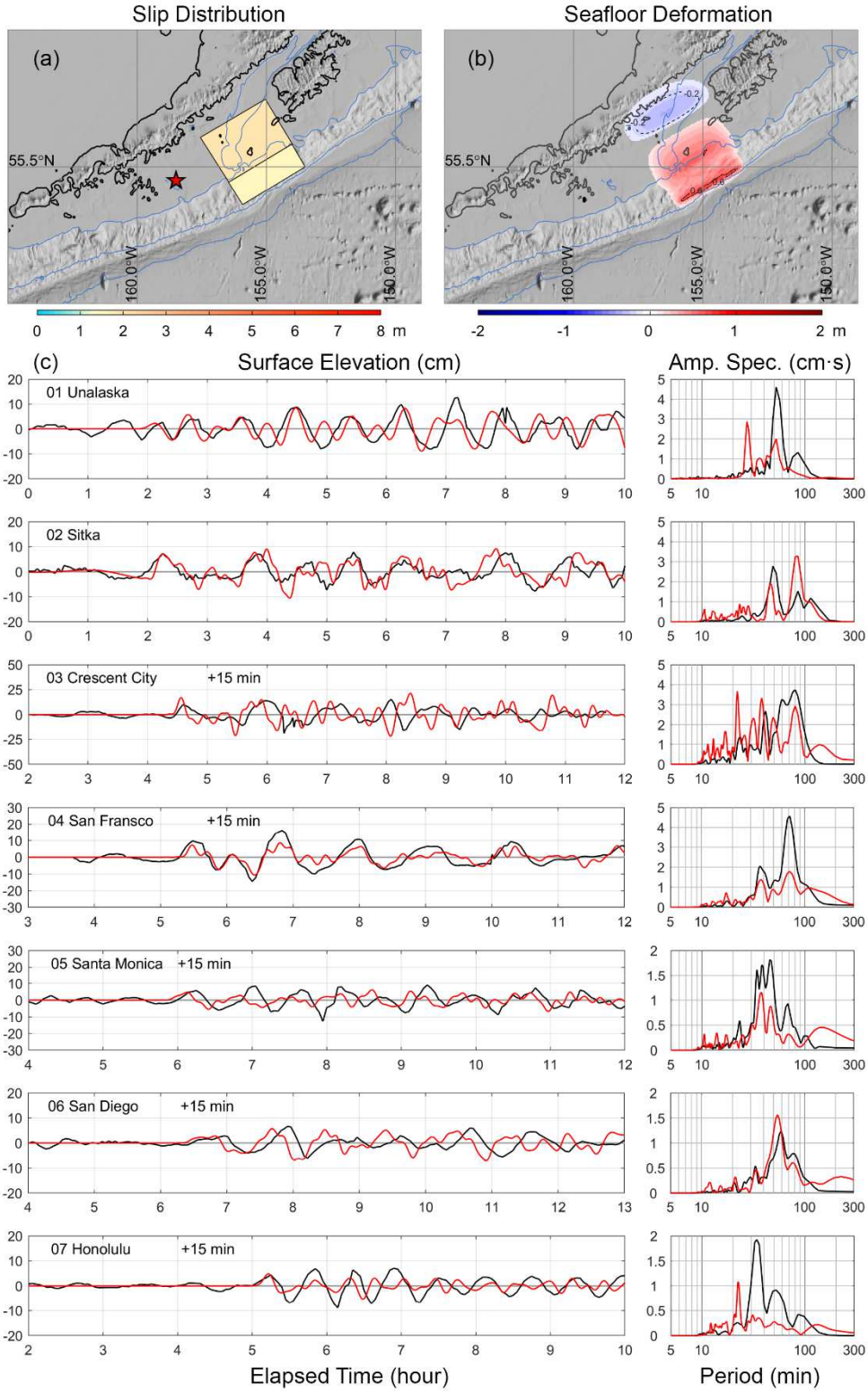

Figure S12. (a) The test model 3 with only 2-m deep slip and 1.5m-shallow slip for the sensitivity of the preferred model in the study, **(b)** corresponding seafloor deformation, and **(c)** comparison of 1938 observed tsunami tide gauge recordings and spectra (black lines) and tsunami calculations for the test model 3 (red lines).

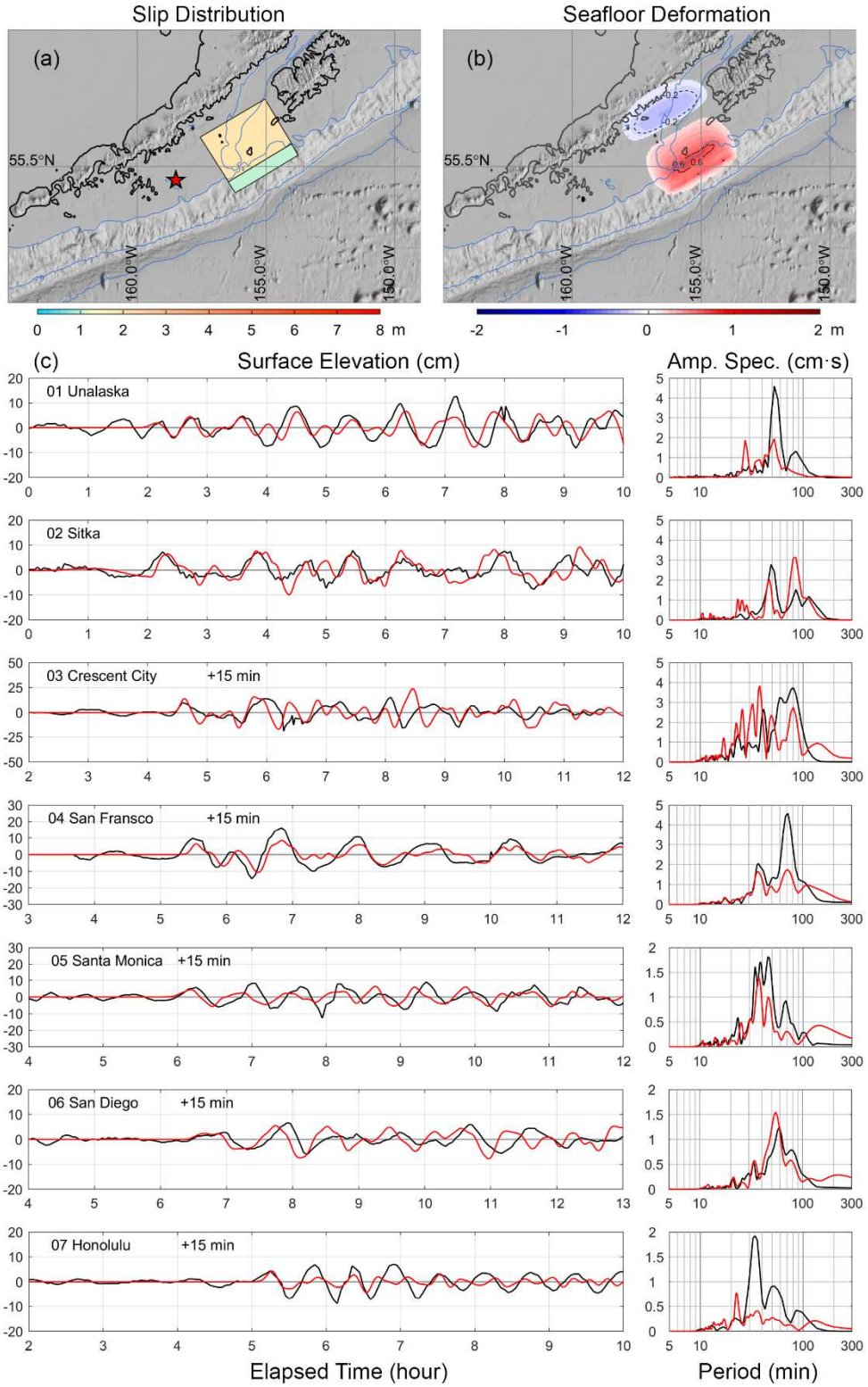

Figure S13. (a) The test model 4 with only 2-m deep slip in full width and 1-m shallow slip in half width for the sensitivity of the preferred model in the study, **(b)** corresponding seafloor deformation, and **(c)** comparison of 1938 observed tsunami tide gauge recordings and spectra (black lines) and tsunami calculations for the test model 4 (red lines).

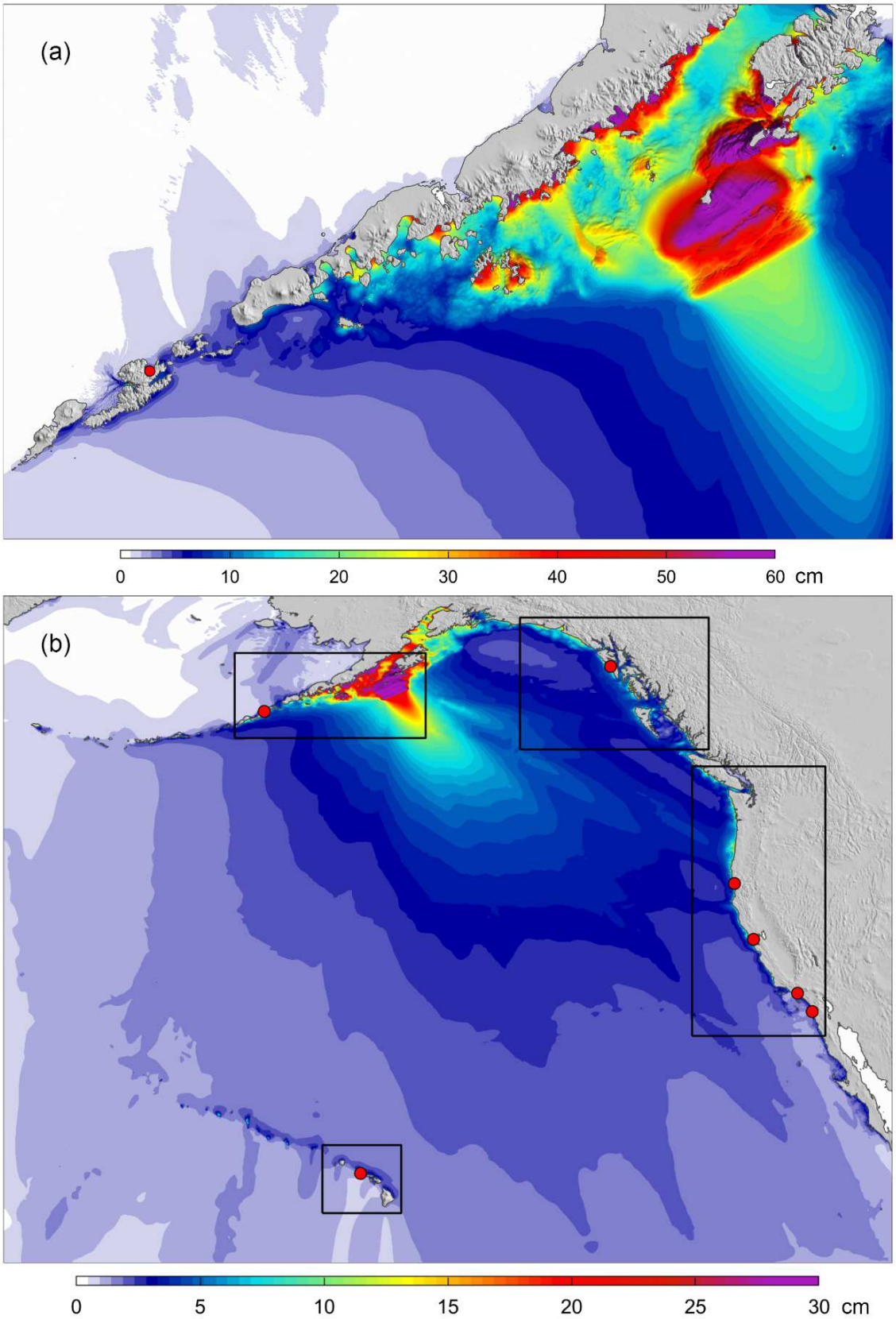

Figure S14. Maps of maximum sea-surface elevation for the preferred 1938 slip model in Fig. 3c in the (a) near-field and (b) far-field.

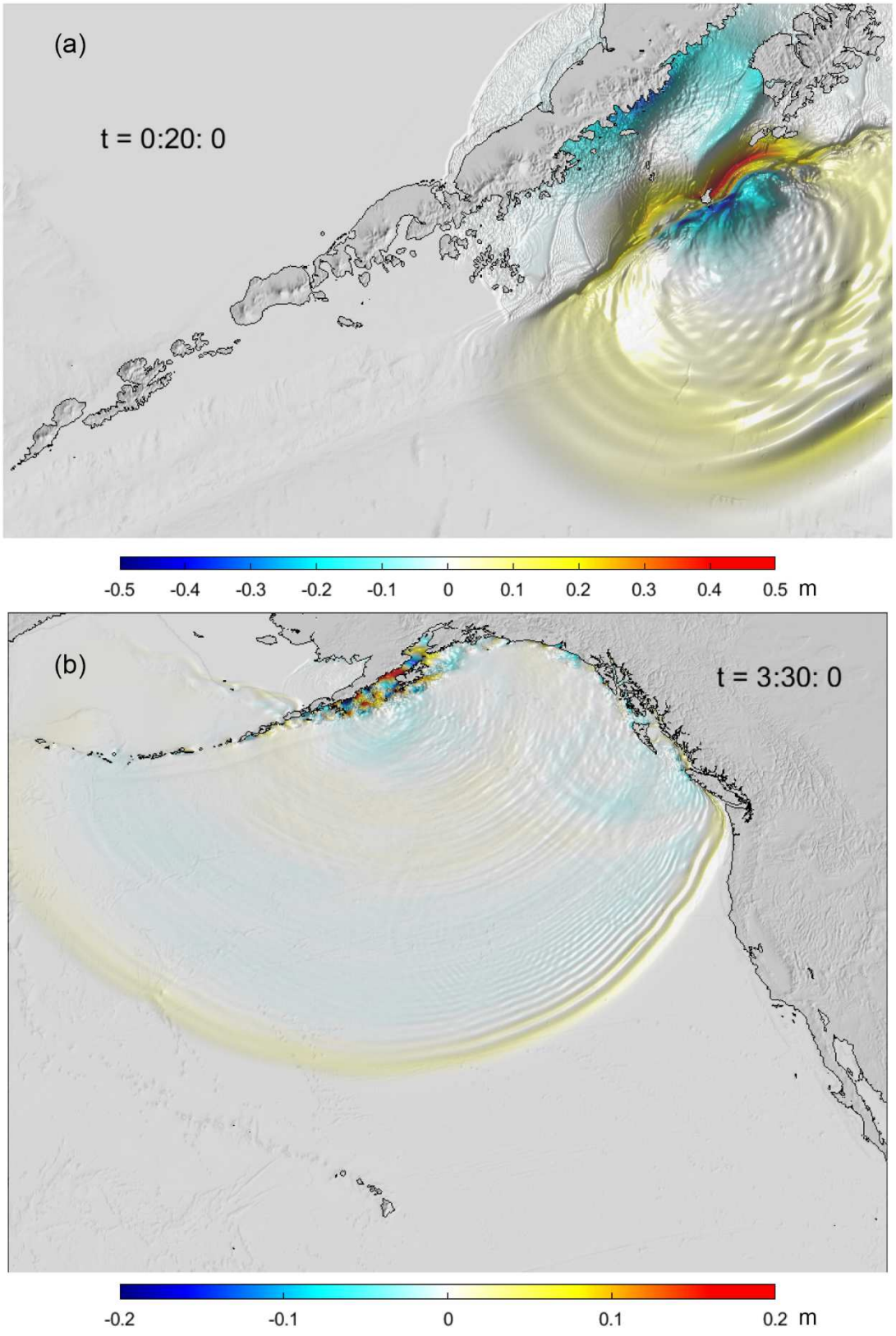

Movies S1 and S2. Animation of sea-surface elevation for the preferred 1938 slip model in Fig. 3c in the (a) near-field and (b) far-field.